





RESEARCH ARTICLE | JANUARY 09 2024

Experimental and numerical investigation on the unsteady interaction in longitudinal stage separation for parallel-staged two-body configuration **FREE**

Special Collection: [Shock Waves](#)

Yue Wang (王粤) ; Yunpeng Wang (汪运鹏)  ; Zonglin Jiang (姜宗林) 



Physics of Fluids 36, 016116 (2024)

<https://doi.org/10.1063/5.0184293>

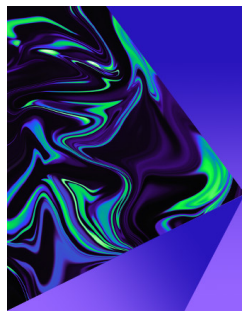


View
Online



Export
Citation

[CrossMark](#)



Physics of Fluids

Special Topic:

Selected Papers from the 2023 Non-Newtonian Fluid Mechanics Symposium in China

Submit Today

Experimental and numerical investigation on the unsteady interaction in longitudinal stage separation for parallel-staged two-body configuration

Cite as: Phys. Fluids **36**, 016116 (2024); doi: 10.1063/5.0184293

Submitted: 25 October 2023 · Accepted: 15 December 2023 ·

Published Online: 9 January 2024






View Online



Export Citation



CrossMark

Yue Wang (王粤),^{1,2}  Yunpeng Wang (汪运鹏),^{1,2,a)}  and Zonglin Jiang (姜宗林)^{1,2} 

AFFILIATIONS

¹State Key Laboratory of High Temperature Gas Dynamics, Institute of Mechanics, Chinese Academy of Sciences, Beijing 100190, China

²School of Engineering Science, University of Chinese Academy of Sciences, Beijing 100049, China

Note: This paper is part of the special topic, Shock Waves.

^{a)}Author to whom correspondence should be addressed: wangyunpeng@imech.ac.cn

ABSTRACT

Hypersonic stage separation is a significant process, probably involving complex aerodynamic interaction, which determines the survival of two-stage-to-orbit (TSTO) vehicles. The longitudinal stage separation (LSS) scheme is proposed to improve the safety of the parallel-staged TSTO vehicle, where a small interstage gap may result in weak interference. Therefore, an experimental and numerical study of LSS for the parallel-staged TSTO vehicle at Mach 7 with different angles of attack (AoA) is carried out. The dynamic interaction, including variations in the shock structure, wall pressure distribution, and unsteady aerodynamics, is investigated by testing and numerical simulation. The LSS experiments for the TSTO vehicle were performed using a high-speed pneumatic ejection launch system in the JF-12 shock tunnel, and the method was developed using high-speed visualization and image processing techniques to capture the separating trajectory. The numerical simulations were carried out using the overset grid method and solving the Navier–Stokes equations coupled with the rigid body dynamics equations to obtain the laminar flows over the TSTO vehicle during LSS. The qualitative and quantitative comparison of the test and numerical results showed good agreement in terms of aerodynamic performance, flowfield pattern, wall pressure, and separation trajectory. They show that the small interstage gap of the LSS leads to weak type I and VI shock–shock interactions, with short-duration weak shock reflection at a higher AoA. Furthermore, no shock reflection or interstage gap is observed at lower AoA. Moreover, no stage recontact is observed, and the safety and feasibility of LSS for parallel-staged TSTO vehicles are demonstrated.

Published under an exclusive license by AIP Publishing. <https://doi.org/10.1063/5.0184293>

I. INTRODUCTION

Two-body configurations are common in aeronautics and astronautics, in which high-speed flows over two-body are inherently complex and important. The parallel-staged two-stage-to-orbit (TSTO) vehicle as a typical two-body configuration is composed of a booster with combined air-breathing propulsion and an orbiter with a rocket engine vehicle.^{1–3} Moreover, the stage separation typically happens in the hypersonic condition, i.e., around Mach 7,¹ so the high-speed flow past a TSTO vehicle such that a two-body system^{4–9} probably include shock wave–shock wave interaction (SSI) and shock wave–boundary layer interaction (SBLI) as well as flow separation.^{10–14} That unsteady flow involves complex aerodynamic interference and multi-body movements causing the TSTO stage

separation to be challenging and determining the safety of the stage separation even a TSTO mission or not.

Due to the separation of two stages with comparable sizes that can mutually affect the aerodynamics of each stage, the analysis of the interstage interaction during the TSTO stage separation is extremely important. The study can be retraced to the Saneger TSTO concept;¹ the prediction of the aerodynamics of stages is a highly challenging problem because of the complex interstage interference, such as the shock wave–vortex interaction. The interaction flowfield pattern at Mach 6.83 for the computational fluid dynamics (CFD) and the wind tunnel test are in good agreement.^{15,16} Cvrlje *et al.*¹⁷ studied the unsteady flow around a TSTO model during stage separation at Mach 6.8. The results showed that unsteadiness should be considered in the

stability during stage separation. Moreover, Schroder *et al.*¹⁸ analyzed the inviscid and viscous hypersonic flows past the Saneger TSTO vehicle at an interstage gap and compared the experimental and numerical data at several relative angles of attack (AoA). Both results showed good agreement in terms of aerodynamic coefficients. Moelyadi *et al.*¹⁹ performed time-dependent simulations of the stage separation considering the effects of unsteady flows since the orbiter's harmonic motions. The results suggested that the unsteady effects must be carefully treated when the orbiter's aerodynamics have a strong change. Bordelon *et al.*²⁰ conducted the wind tunnel test to examine the TSTO stage separation flowfield at Mach 2.74–4.96; the results showed that the shock wave plays a big role in the aerodynamics and the vehicle could be statically unstable at some positions during separation. Ozawa *et al.*²¹ studied the flow past the hemisphere-cylinder/flat-plate TSTO configuration at Mach 8.1 under different interstage gaps. The results showed that the flowfield would be unsteady at a certain interstage gap, and high pressure and thermal loads are induced by the SSI. Gong *et al.*²² numerically studied the unsteady aerodynamic characteristics of the TSTO vehicle during stage separation and analyzed the possible safe separation conditions. In addition, they verified the numerical results with dual-body synchronous captive trajectory test (CTS) results.²³ The results showed a very small margin for safe TSTO separation. Wang *et al.*²⁴ numerically studied the separation of two-body configurations at Mach 7, and the flow patterns and the aerodynamic interference were analyzed. The results showed that the interference tends to be stronger with the higher interstage incidence angle but tends to be less strong with increasing the interstage clearance. Moreover, Wang *et al.*⁸ numerically investigated the unsteady interaction mechanism involving the effects of the center of gravity for the TSTO vehicle at Mach 6.7; their results showed that the pitching moment of the orbiter, which is influenced by the interstage SBLI and SSI, dominates the separation safety.

These studies have exposed the problem that strong aerodynamic interference occurs when the notable and varying interstage gap is happening to the TSTO during separation. The stage separation scheme, in which the orbiter separates from the booster in the normal direction, can be named transverse stage separation (TSS).²⁵ In addition, an alternative separation scheme was proposed by Wang *et al.*,^{25,26} i.e., longitudinal stage separation (LSS), for parallel-staged TSTO vehicles. The orbiter separates along the upper wall of the booster under the thrust of the rocket engine, with tiny or even no gap, which may result in weak aerodynamic interference.²⁷ Wang *et al.*^{28,29} have conducted the free-flight experimental test of LSS for the parallel-staged TSTO vehicle at Mach 7 in the JF-12 duplicate flight condition shock tunnel (JF-12 shock tunnel), which is the first report of the free-flight active stage separation for the parallel-staged TSTO vehicle in the hypersonic wind tunnel. The test verified the principle of the LSS scheme for the parallel-staged TSTO vehicle. However, due to the finite and limited flow results during free-flight testing that were measured and observed in the shock tunnel, the CFD simulation of LSS for the TSTO vehicle at the same freestream conditions is conducted to analyze the unsteady flowfield in depth. In addition, the flow pattern, the unsteady wall pressure, and the separation trajectory are going to be compared together between the CFD and experimental results to deeply reveal the aerodynamic interference and flow mechanism of the LSS and also validate the reliability and the accuracy of the numerical simulation, and vice versa.

II. TSTO MODEL

The parallel-staged TSTO model for testing and CFD simulations consists of a waverider and a spaceplane as the booster and the orbiter respectively, and the detailed TSTO concept, configuration, and related works can be depicted in these studies.^{26–28} Figure 1 presents the size of the TSTO model, and the coordinate system origin is set on the nose of the booster. The length of the booster is $l_b = 1$ m, and its center of gravity (CG) is located at (0.738, -0.05, 0) m. The length of the orbiter is $l_o = 0.4$ m, and its CG is located at (0.740, 0.016, 0) m. Figure 2 shows the photo of the tested TSTO model in the JF-12 shock tunnel test section and associated devices for the dynamic stage separation. The AoA of the TSTO vehicle is defined as the relative angle between the airflow and the booster's upper surface. In the testing, the AoA is adjusted by the angle between the model strut and the pedestal in the test section, while in the CFD simulation, it is adjusted by the components of the inflow velocity and the TSTO model sets horizontally. As shown in Fig. 2, in the testing, the booster is equipped on the model strut by the six-component strain-gauge balance. Additionally, the orbiter moves along the booster's upper surface with enough high impulse, in which high-pressure nitrogen pushes the cylinder to do work and transfers the impulse to the orbiter by the impact bar. Thus, the dynamic test of LSS is carried out in that way in the JF-12 shock tunnel. The TSTO model is mainly made from aluminum alloy materials. For the CFD simulations and testing, the non-dimensional mass of the orbiter is $m_o/\rho_\infty l_o^3 = 3175$, and the moments of inertia are $I_{xx}/\rho_\infty l_o^5 = 21$, $I_{yy}/\rho_\infty l_o^5 = 210$, and $I_{zz}/\rho_\infty l_o^5 = 198$. Herein, $\rho_\infty = 0.0062 \text{ kg}\cdot\text{m}^{-3}$ refers to the density of freestream. The mass characteristics of the orbiter model are assessed by computer-aided engineering (CAE) software. Moreover, the booster is assumed to be fixed, while the orbiter separates from the booster with an appropriate initial velocity in simulations. The orbiter yields six degrees of freedom (6-DOF) motion equations under the aerodynamic forces and moments as well as gravity force. The reference point for the moments is located on the CG. In addition, the separation device between the two stages in the testing shown in Fig. 2 is omitted in the simulations.

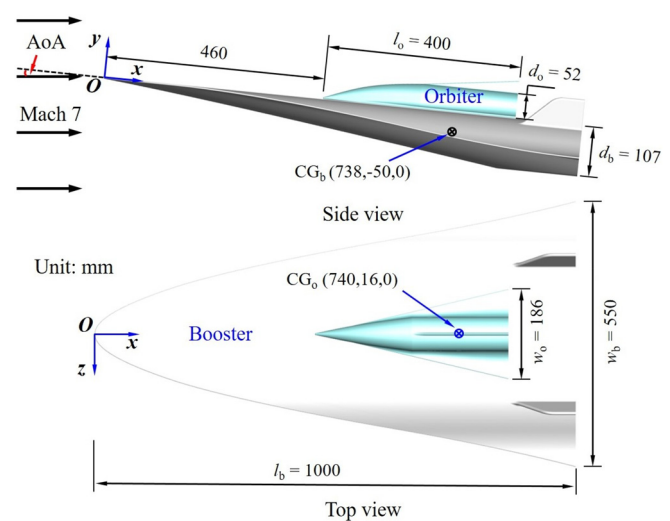


FIG. 1. The overall size of the scaled TSTO model.

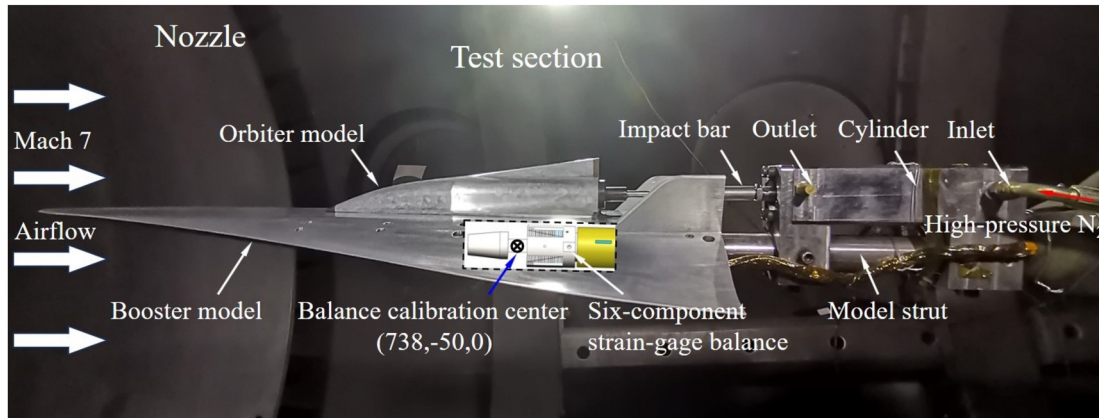


FIG. 2. The TSTO test model in the test section of the JF-12 shock tunnel.



FIG. 3. The photo of the JF-12 shock tunnel.

III. EXPERIMENTAL AND NUMERICAL PROGRAM

A. Experimental program

1. Test facility and conditions

A series of tests for the parallel-staged TSTO vehicle model are conducted in the JF-12 shock tunnel at the Institute of Mechanics. The JF-12 is the long-test-duration hypersonic detonation-driven shock tunnel that is developed based on the backward-running detonation driver with several innovative techniques.^{30–32} JF-12 shock tunnel consists of a damping section, a detonation chamber, a shock tube, a

nozzle, and a test section. Figure 3 presents the photo of the JF-12 shock tunnel. The overall length of the JF-12 shock tunnel is 265 m and its test section with a diameter of 3.5 m and a length of 11 m. JF-12 can reproduce the pure airflow with Mach 5–9 at an altitude of 25–50 km with at least 100 ms effective test time. Since the reproducing test airflow covers the TSTO stage separation condition and large test section for free-flight large-scale multibody separation test, the JF-12 shock tunnel suits for the dynamic stage separation test for the TSTO vehicle very well. The nozzle with an exit diameter of 2.5 m is employed to generate the nominal Mach 7 airflow. Table I shows the detailed reproduced hypersonic freestream conditions for different tests of the TSTO vehicle.

2. Measurement methods

In the test, a series of measurement methods include a high-speed visualization system (Schlieren and camera), wall pressure, static forces and moments, and separating trajectory capturing for the TSTO vehicle. Figure 4 shows the sketch of the high-speed visualization system incorporated into the JF-12 shock tunnel, which consists of a high-speed Schlieren camera I with a frame rate of 3600 fps and a high-speed camera II with a frame rate of 1000 fps. The Schlieren camera captures the shock wave structure for the TSTO vehicle in the observation window and the high-speed camera II captures the separating process from the rear side view. Moreover, several light emitting diodes (LEDs) are equipped on the right sidewall as the markers in the Schlieren video for capturing the separation trajectory and the capturing method will be introduced in the next section. Figure 5 shows the pressure sensors and a six-component strain-gauge balance.

TABLE I. Test airflow conditions.

No.	Test case	AoA (deg)	p_0 (MPa)	T_0 (K)	H_0 (MJ·kg ⁻¹)	Ma_∞	Re_∞ (m ⁻¹)	p_∞ (Pa)	ρ_∞ (kg·m ⁻³)	U_∞ (m·s ⁻¹)
1	Booster	5.0	2.50	2364	2.71	6.95	8.47×10^5	447	0.0062	2215
2	TSTO	8.1	2.46	2378	2.72	6.93	8.33×10^5	448	0.0061	2221
3	LSS free-flight	8.3	2.63	2393	2.74	6.99	8.57×10^5	451	0.0062	2231
4	LSS free-flight	4.5	2.53	2371	2.71	6.95	8.55×10^5	454	0.0062	2218

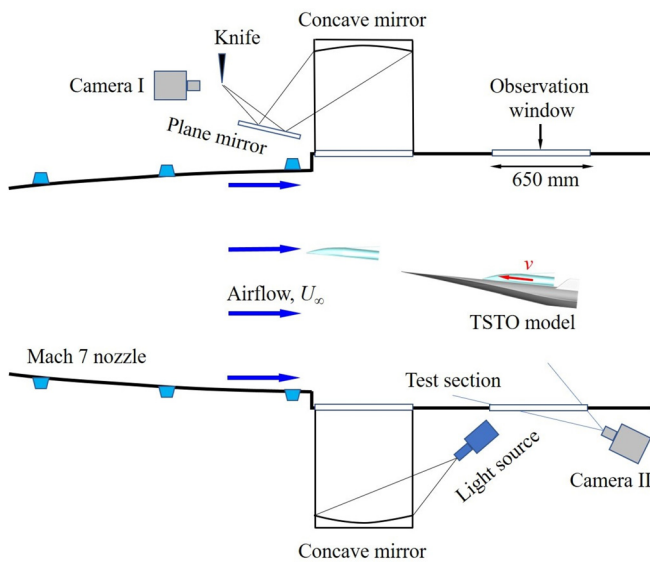


FIG. 4. The sketch of the high-speed visualization system in the JF-12 shock tunnel.

The pressure along the symmetry lines on the booster’s upper and lower walls is measured by the pressure sensors with a range of 50 kPa and an accuracy of 0.25% F.S. (Full scale). The sampling rate is 100 kHz. In addition, a pitot pressure sensor is installed at the exit of the nozzle to measure the airflow conditions. The forces and moments exerted on the booster are measured by the six-component strain-gauge balance, which forms an integral structure with the sting-model support system,^{33,34} and the balance calibration center is on the booster’s CG as shown in Fig. 2. Moreover, the capacities of the balance to the axial and normal forces as well as the pitching moment are 1000, 2000, and 200 N·m, respectively. The sampling rate is 50 kHz.

3. Free-flight LSS methodology

The free-flight multibody separation experimental test in the hypersonic wind tunnel is few, let alone in the shock tunnel. Several challenging problems block in front of the free-flight LSS test for such a scale TSTO vehicle in the JF-12 shock tunnel but they are solved by the corresponding methodology as follows: first, too short effective test duration, i.e., about millisecond scale; second, separation trajectory

capturing; third, unsteady aerodynamics measurement and identification; and last, free-flight model’s damage. Although the JF-12 is a long-test-duration shock tunnel with at least 100 ms, it is too challenging to make the orbiter model with a mass of 1.26 kg to finish the LSS in the length scale around 1 m within 100 ms. In a word, the orbiter would separate with a flight speed of around $10 \text{ m}\cdot\text{s}^{-1}$ in the test section, which is hard. To meet the requirement, the high-speed pneumatic ejection to launch vehicle model system (HPELS) is developed and incorporated into the operation of the JF-12 shock tunnel. Figure 2 presents the core components of the HPELS. In the LSS test, the high-pressure nitrogen with around 8 MPa acts as the working fluid to drive the cylinder for imposing the orbiter model a great initial impulse so that the orbiter can separate from the booster within 100 ms. With the appropriate and precise timing control of the HPELS, the orbiter can separate from the booster with an average speed of $8\text{--}13 \text{ m}\cdot\text{s}^{-1}$ in the test. Detailed information on the constitute elements and control of the HPELS was recorded in the previous study.²⁸ Figure 6 presents the time history of the voltage of the pitot pressure and the schematic of timing sequences of the dynamic tests in the JF-12 shock tunnel. The time indicated in Fig. 6 is defined and explained as follows. The operation (i.e., ignition) of the JF-12 shock tunnel, HPELS, and the data acquisition system (i.e., pressure, heat flux, Schlieren, high-speed camera, etc.) are triggered at the same time. However, due to the complexity of the LSS test, the delay time is needed and overall coordinated. The ignition of the JF-12 shock tunnel is delayed by about 488 ms (T_i) to wait for the HPELS act delay time (T_d). T_{td} is the HPELS trigger delay time and is set by the signal controller. In the dynamic test, T_d and T_{td} should be carefully calibrated and determined along with the orbiter advance movement time (T_a) to achieve the ideal observation for the LSS test. The practical timing sequences for the LSS test operation corresponding to Fig. 6 are presented in Table II. Figure 7 shows the schematic of the LSS test; it can be divided into three phases: I. from the initial position “A” to the position “B” where the nose of the two stages coincides, II. from the position “B” to the position “C” where the tail of the orbiter and the nose of the booster coincides, and III. orbiter separates from the booster and flights freely. The ideal observation for the LSS test is that the significant process from “B” to “C” is at least investigated during the effective test duration (T_e).

The observation window of the JF-12 test section is big enough to capture most of the LSS motion with a diameter of 650 mm as shown in Fig. 4. Since the complexity and limitations of the motion data acquired by sensors for moving model, those data are acquired by postprocessing the separation trace results. Several LEDs equipped on the orbiter orientate vertically to the observation window. Therefore,

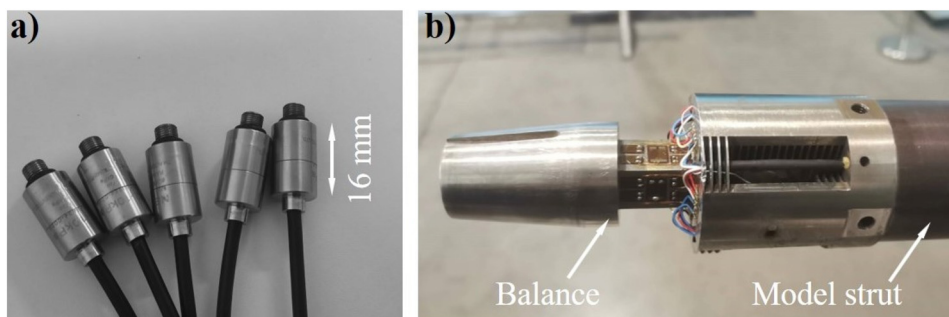


FIG. 5. The pressure sensors (a) and six-component strain-gauge balance (b).

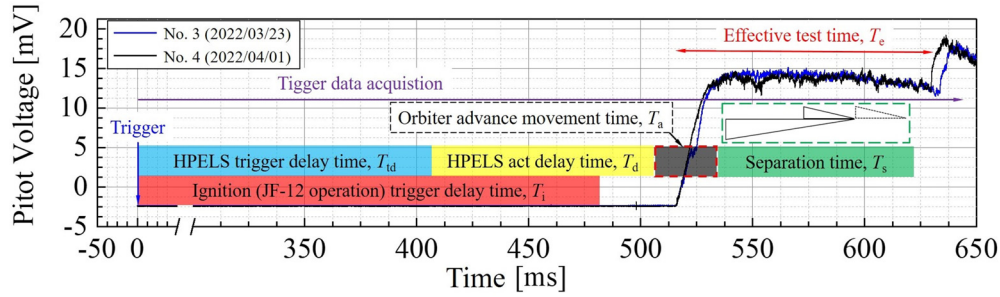


FIG. 6. Pitot pressure voltage and schematic of timing sequences of the dynamic tests in the JF-12 shock tunnel.

TABLE II. Timing sequences for LSS tests.

No.	Test case	T_i (ms)	T_{td} (ms)	T_d (ms)	T_e (ms)
3	LSS free-flight	488	370	79	115
4	LSS free-flight	488	470	86	117

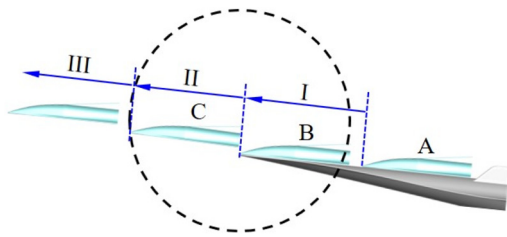


FIG. 7. Schematic of the LSS test.

LEDs that show a white faculae in the Schlieren video can be identified clearly and easily by the image recognition method (as shown in Fig. 8), and then the orbiter’s trajectory and pitching angle can be acquired. The non-contact trajectory trace method is cheap, practical, and has minor effects on the dynamic test results because its structure is very lightweight.

The separating trajectory and the pitching angle of the orbiter in the Schlieren video are captured as follows. Before the test, the length of each LED from the orbiter’s CG (l_i), the sharp angle formed by the connecting line of each LED and the orbiter’s CG and the horizontal

line (φ_i), and the diameter of the observation window D_w are known. After recognizing the LED’s pixel coordinate (x_{ip}, y_{ip}) in the Schlieren photo in every frame, these pixel coordinates should be transferred into the spital coordinates (x_i, y_i) in the established coordinate system as shown in Fig. 1. Before the calculation, the pixel coordinate length of the diameter of the observation window D_p is measured in the Schlieren photo; then, the orbiter’s CG coordinate and its pitching angle in one frame instant t_j and the last frame instant t_{j-1} based on the Schlieren video can be acquired as follows. First, using the least squared method to determine the slopes k_j and k_{j-1} of the straight line fitted by the LEDs (x_{ip}, y_{ip}) at the instant t_j and the last instant t_{j-1} . Then, determine the relative variation value of the angles in the two instants by the two slopes

$$\Delta\theta_j = \tan^{-1}|k_j| - \tan^{-1}|k_{j-1}|. \quad (1)$$

Next, accumulating and summing these relative angle between the instant t_j and the initial instant when the orbiter is going to appear in the observation window, and the orbiter’s pitching angle at the initial instant in the Schlieren video is measured artificially as α (α is usually a small quantity near or equal to zero). Therefore, the orbiter’s pitching angle at the instant t_j is calculated as

$$\theta_j = \sum_{j=1}^j \Delta\theta_j + \alpha (j = 1, 2, 3 \dots). \quad (2)$$

The pixel coordinate of the origin of the established physical coordinate system in the Schlieren photo is (x_{op}, y_{op}); then, the coordinate of each LED at the instant t_j during the separation is

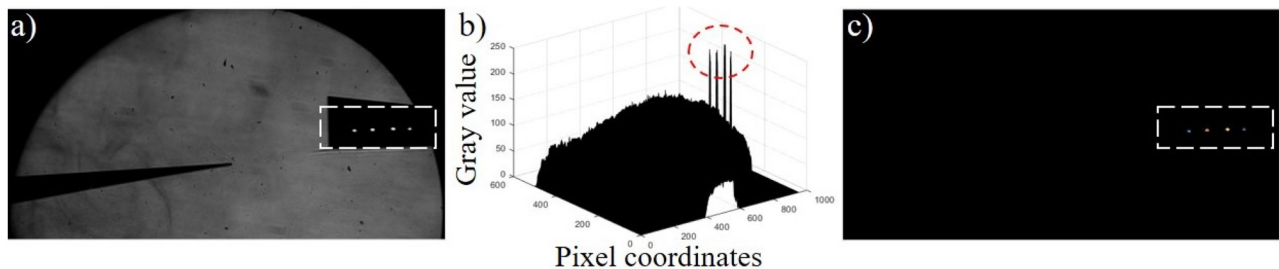


FIG. 8. Recognition of LEDs’ pixel coordinates on the orbiter model based on the Schlieren image: (a) gray photo of the Schlieren image, (b) the distribution of the gray value, and (c) identification of the LEDs’ pixel coordinates.

$$x_i = (x_{op} - x_{ip})D_w/D_{wp}, \quad y_i = (y_{op} - y_{ip})D_w/D_{wp}. \quad (3)$$

So, the coordinate of the orbiter's CG at the instant t_j is

$$x_{cg} = \frac{\sum_{i=1}^n x_i \pm l_i \cdot \cos(\varphi_i \pm \theta_j)}{n}, \quad y_{cg} = \frac{\sum_{i=1}^n y_i \pm l_i \cdot \sin(\varphi_i \pm \theta_j)}{n}. \quad (4)$$

In Eq. (4), when the LED is located upstream of the orbiter's CG, the sign is plus, and the else is minus. Additionally, n is the amount of the LEDs observed in the Schlieren video.

Due to the strong strike to the test model in the pulse shock tunnel, the measured signals of the balance in the dynamic test include the forced vibration signal, the low-frequency inertial signal, and noisy as well as unsteady aerodynamics signal.^{33,34} It is too hard to extract unsteady aerodynamic components accurately from such complex balance signals. To acquire the unsteady aerodynamics of TSTO during the LSS, the numerical aerodynamics are computed from the corresponding reliable and validated CFD simulations of hypersonic flows past the TSTO vehicle during LSS for subsequent discussion and analysis. Moreover, the static aerodynamics can be accurately obtained for TSTO in the aerodynamics performance tests (i.e., No. 1 and 2 test cases) by averaging the aerodynamics measured by the balance during the effective test duration.

Since the orbiter model is separating from the booster during LSS tests and the waves and flows in the JF-12 shock tunnel after the effective test duration are strong and complex, the falling point of the free-flight orbiter model cannot be predicted accurately resulting in the orbiter model that cannot be protected and recycled. Moreover, the recycling and protection device for the orbiter model probably have interference effects on the airflow and TSTO flowfield. Therefore, the orbiter model in every dynamic test is disposable, and several orbiter models are prepared for the tests. Figure 9 presents several damaged orbiter models in the free-flight tests.

B. Numerical program

1. Govern equations and numerical methods

Since the finite and limited experimental data can be measured by the free-flight LSS tests in the shock tunnel, the unsteady CFD simulations of solving the Navier–Stokes (N–S) equations and the six-degree-freedom (6-DOF) rigid body dynamics equations for LSS of the

TSTO are performed to compare and analyze together with the test data in detail.

The unsteady three-dimensional (3-D) N–S equations employed for the simulation of the dynamic TSS of the TSTO are given by

$$\frac{\partial}{\partial t} \iiint_{\Omega} W d\Omega + \iint_{\partial\Omega} (F_c - F_v) dS = 0, \quad (5)$$

where W , F_c and F_v are the vectors of conservative variables, convective fluxes, and viscous fluxes, respectively, which are expressed as

$$W = \begin{pmatrix} \rho \\ \rho u \\ \rho v \\ \rho w \\ \rho E \end{pmatrix}, \quad F_c = \begin{pmatrix} \rho V_r \\ \rho u V_r + n_x p \\ \rho v V_r + n_y p \\ \rho w V_r + n_z p \\ \rho H V_r + V_g p \end{pmatrix}, \quad (6)$$

$$F_v = \begin{pmatrix} 0 \\ n_x \tau_{xx} + n_y \tau_{xy} + n_z \tau_{xz} \\ n_x \tau_{yx} + n_y \tau_{yy} + n_z \tau_{yz} \\ n_x \tau_{zx} + n_y \tau_{zy} + n_z \tau_{zz} \\ n_x \Theta_x + n_y \Theta_y + n_z \Theta_z \end{pmatrix},$$

where ρ is the density, u , v , and w are the velocity components in the x , y , and z directions, respectively, p is the pressure, and E and H are the total energy and the total enthalpy per unit mass. Moreover, $p = (\gamma - 1)[\rho E - 1/2\rho(u^2 + v^2 + w^2)]$ and $H = E + p/\rho$, where γ is the specific heat ratio; τ_{ij} is the component of viscous stress; Θ_x , Θ_y , and Θ_z are the heat conduction; n_x , n_y , and n_z are the components of the unit outward-facing normal vector; V_r represents the contravariant velocity relative to the motion of the grid, which is expressed as

$$V_r = V - V_g = (u - u_g)n_x + (v - v_g)n_y + (w - w_g)n_z, \quad (7)$$

where $V_g = u_g n_x + v_g n_y + w_g n_z$ is the contravariant velocity at the surface of the control volume. To close the system of equations, the ideal gas equation of state is introduced: $p = \rho RT$. Additionally,

$$\Theta_x = u\tau_{xx} + v\tau_{xy} + w\tau_{xz} + k_T \frac{\partial T}{\partial x}, \quad (8)$$



FIG. 9. The damaged orbiter models in the tests.

$$\Theta_y = u\tau_{yx} + v\tau_{yy} + w\tau_{yz} + k_T \frac{\partial T}{\partial y}, \quad (9)$$

$$\Theta_z = u\tau_{zx} + v\tau_{zy} + w\tau_{zz} + k_T \frac{\partial T}{\partial z}, \quad (10)$$

where k_T is the coefficient of thermal conductivity and T is the temperature. The components of the viscous stress tensor are obtained from the following relations:

$$\tau_{xx} = 2\mu \frac{\partial u}{\partial x} - \frac{2}{3}\mu \left(\frac{\partial u}{\partial x} + \frac{\partial v}{\partial y} + \frac{\partial w}{\partial z} \right), \quad (11)$$

$$\tau_{yy} = 2\mu \frac{\partial v}{\partial y} - \frac{2}{3}\mu \left(\frac{\partial u}{\partial x} + \frac{\partial v}{\partial y} + \frac{\partial w}{\partial z} \right), \quad (12)$$

$$\tau_{zz} = 2\mu \frac{\partial w}{\partial z} - \frac{2}{3}\mu \left(\frac{\partial u}{\partial x} + \frac{\partial v}{\partial y} + \frac{\partial w}{\partial z} \right), \quad (13)$$

$$\tau_{xy} = \tau_{yx} = \mu \left(\frac{\partial u}{\partial y} + \frac{\partial v}{\partial x} \right), \quad (14)$$

$$\tau_{xz} = \tau_{zx} = \mu \left(\frac{\partial u}{\partial z} + \frac{\partial w}{\partial x} \right), \quad (15)$$

$$\tau_{yz} = \tau_{zy} = \mu \left(\frac{\partial v}{\partial z} + \frac{\partial w}{\partial y} \right), \quad (16)$$

where μ is the viscosity coefficient.

The 6-DOF rigid body dynamic (RBD) motion is governed by

$$m \left(\frac{dV_x}{dt} - V_y\omega_z + V_z\omega_y \right) = F_x, \quad (17)$$

$$m \left(\frac{dV_y}{dt} - V_z\omega_x + V_x\omega_z \right) = F_y, \quad (18)$$

$$m \left(\frac{dV_z}{dt} - V_x\omega_y + V_y\omega_x \right) = F_z, \quad (19)$$

$$I_{xx} \frac{d\omega_x}{dt} - (I_{yy} - I_{zz})\omega_y\omega_z = M_x, \quad (20)$$

$$I_{yy} \frac{d\omega_y}{dt} - (I_{zz} - I_{xx})\omega_z\omega_x = M_y, \quad (21)$$

$$I_{zz} \frac{d\omega_z}{dt} - (I_{xx} - I_{yy})\omega_x\omega_y = M_z. \quad (22)$$

Equations (13)–(15) represent the translation of the CoG of the body, and Eqs. (16) and (17) represent the rotation of the CoG in the body's axial system, where m is the mass of the body, V_x , V_y , and V_z are the velocity components of the body (also the velocity of the orbiter grid), ω_x , ω_y , and ω_z are the components of the angular velocity of the body, F_x , F_y , and F_z are the components of the applied force exerted on the body, including aerodynamic forces and gravity. Where I_{xx} , I_{yy} , and I_{zz} are the principal moment of inertia of the body, and M_x , M_y , and M_z are the components of the applied moment exerted on the body.

The three-dimensional N–S equations are solved by the finite volume method.³⁵ A second-order total variation diminishing (TVD) polynomial interpolation scheme with a minmod limiter is used for spatial discretization.³⁶ The Harten–Lax–van Leer contact (HLLC) approximation Remann scheme is used to compute convective flux,³⁷ and the viscous flux terms are evaluated by the second-order simple average of all the vertex polynomials. Additionally, the coefficient of

viscosity and thermal conductivity are evaluated by Sutherland's law. Time advancement is performed by the implicit backward Euler integration with multi-grid acceleration and dual time step method.³⁸ In the couple computation of the N–S solver and 6-DOF motion for the separation of the TSTO, the movement of the orbiter can be updated by solving 6-DOF equations with the fourth-order Runge–Kutta advancing method after the integrated aerodynamics acts on the orbiter are computed from the flow solver. Next, the new relative position of the two stages is updated. Thus, the new aerodynamics on the orbiter can be computed from the flow solver again at a new time step. The freestream conditions for different cases are the same as the corresponding tested airflow conditions that are presented in Table I. Since the small Reynolds number of freestream, the laminar flow simulations are adopted. Moreover, the laminar flow within 1 m has not been transitioned into the turbulent flow in such an airflow condition, which has been validated by the experiment conducted in the JF-12 shock tunnel.³⁹ In addition, the rarefied gas effects and nonequilibrium real gas effects^{40,41} are not included and considered in the current study because of the relatively low total enthalpy $H_0 < 5 \text{ MJ}\cdot\text{kg}^{-1}$ and a sufficiently small Knudsen number of $1.2 \times 10^{-5} < 0.05$; they would be notable and play roles in the very hypervelocity and higher enthalpy flow ($H_0 > 5 \text{ MJ}\cdot\text{kg}^{-1}$) sceneries.^{42–44} Thus, the freestream gas property is considered as the calorically perfect gas. Moreover, some finished studies done by Schroder *et al.*^{16,18} have shown that the perfect-gas laminar flow simulation for hypersonic flow over the TSTO vehicle is reliable. In the simulations, all conservative variables at the inflow boundary and flowfield initialization are determined by the JF-12 airflow conditions as shown in Table I. The conservative variables at the outflow boundary are computed from the solution in the computational domain (centroidal extrapolation). The non-slip and adiabatic conditions are adopted on the wall boundary. In terms of starting the LSS in the CFD simulations, the orbiter would be separated from the booster with an initial separating speed of $8.5 \text{ m}\cdot\text{s}^{-1}$ and $13.3 \text{ m}\cdot\text{s}^{-1}$ corresponding to the free-flight test of Nos. 3 and 4, respectively, and then the orbiter is subjected to the aerodynamics, gravity, and supporting force by the booster's upper surface. Moreover, the mass characteristics of the orbiter are the same as the test model condition as described in Sec. II.

2. Overset grid

Since the function and efficiency of the overset grid methodology on solving the flowfields involving the multibody movement, it is used for computing the LSS flowfields for the TSTO vehicle.⁴⁵ Figure 10 presents the computational overset grid for the TSTO vehicle and the sketch of the boundary conditions used in the simulations. The overset grid is composed of two sub-grids, i.e., the booster grid as a background grid and the orbiter grid as a moving grid. Both sub-grids are generated by the hybrid meshing method and comprise structured and unstructured blocks. The first cell spacing normal to the wall is chosen to ensure $y^+ \sim 1$ and a progression ratio of 1.1 is applied to cluster grid points radially outward from the wall as well as 40 cells spanned the thickness of the boundary layer to capture the appropriate boundary layer flow. The overset method applied to the computation of the TSTO separation involves the connection of the two sub-grids, i.e., booster grid and orbiter grid, by hole cutting and data interpolation at every time step. The flow data are exchanged and interpolated on the overset cells between two sub-grids to achieve second-order accuracy

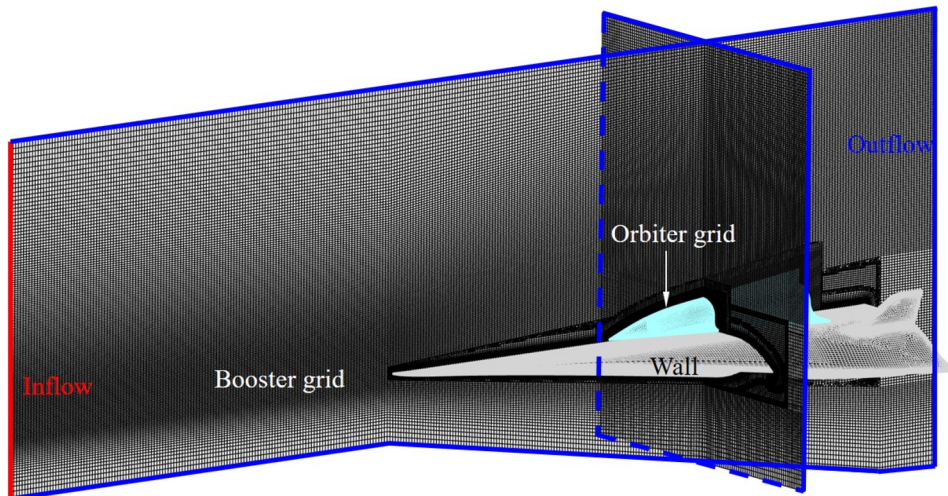


FIG. 10. The schematic of the computational overset grid for the TSTO vehicle.

within two or more layers of interpolated grid nodes. During stage separation, the sub-grids remain unchanged, but the overset grid is updated with the movement of the orbiter at every time step. The flow data are exchanged between sub-grids during the flowfield construction and computation. In a series of previous studies, the computational grid and the time step resolution requirements for the simulations of the TSTO stage separation were validated.^{26,27} In the present study, a grid size of about 14 million cells can provide an acceptable numerical result with a computational time step of $dt \cdot U_\infty / l_b = 0.2131$, where dt is the dimensional time step and $U_\infty = 2231 \text{ m} \cdot \text{s}^{-1}$ is the freestream speed to obtain reliable unsteady flowfield with computational efficiency and acceptable cost. Furthermore, the computed LSS flowfields are going to be compared to the test results to show their reliability.

3. Validations

The SBLI and the multibody 6-DOF motion are the typical characteristics of the multibody separation in high-speed flow, so these associated typical flowfield simulation cases should be carried out to

validate the reliability and efficiency of the numerical methods. In the study, the shock wave-laminar boundary layer interaction⁴⁶ and the wing-pylon-store separation⁴⁷ cases in the literature were validated to determine the reliability of the same numerical methods for computing the hypersonic flowfield of the TSTO stage separation. The experimental data from the Mach 12.2 hypersonic laminar flows over the double-cone model in the LENS XX hypersonic wind tunnel⁴⁶ and Mach 1.2 supersonic flows over the wing-pylon-store separation⁴⁷ were compared to the corresponding CFD simulation results. Figure 11 shows the computational and experimental results of the hypersonic flows over the double cone model. The difference in the peak pressure between the CFD and the experiment is observed due to the complex separated and reattached flow region. However, the separation region and the wall pressure distribution tendency are consistent between both results. Figure 12 presents the computational and experimental results of the wing-pylon-store separation. The computational overset grid with total cells of 8.5 million is shown in Fig. 12(a); the time history of the displacements and Euler angles are in good agreement except for the disparity of the roll angle in the later stage. That is probably because the accumulated computational error of the roll moment

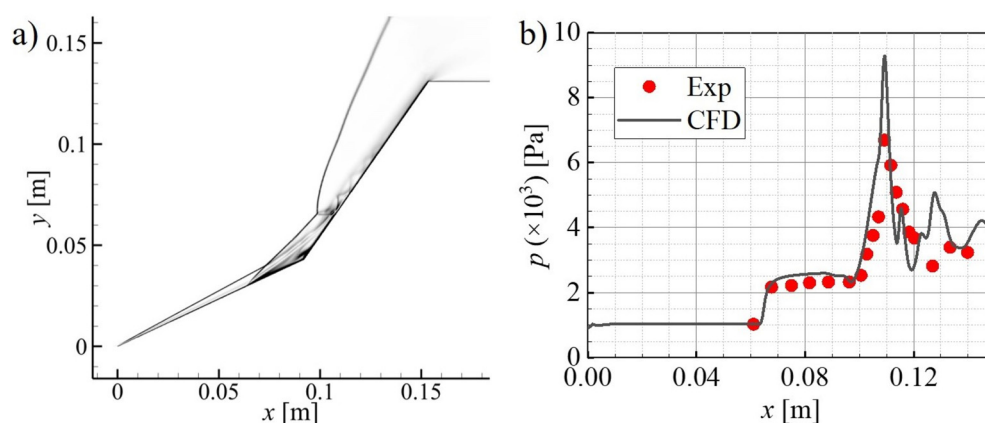


FIG. 11. The computational flowfield of hypersonic flows over the double-cone (a) and comparison of the computational and experimental wall pressure distribution (b).

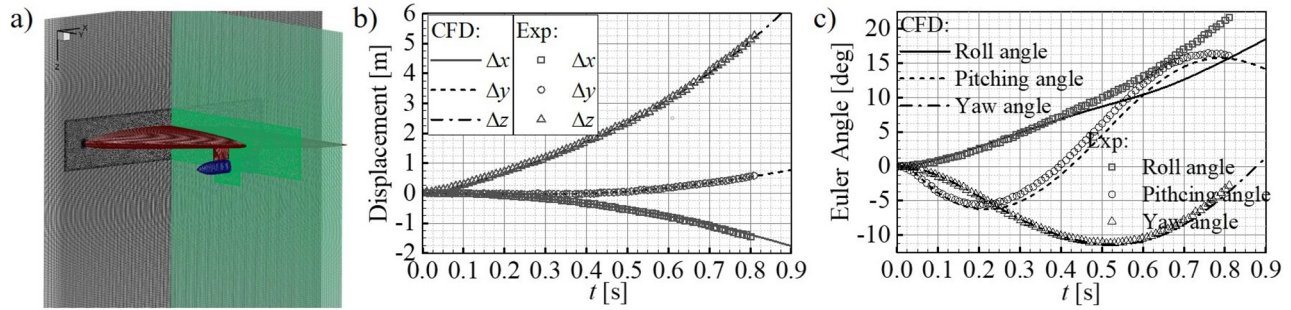


FIG. 12. The computational grid of the wing-pylon-store model (a), comparison of the computational and experimental store's displacements (b), and Euler angles (c).

relative to the experiment was gradually amplified since the relatively small moment of inertia of the store in the roll direction. In general, the computational method applied here can accurately capture the store separation behavior. In conclusion, the comparison of those two cases can validate the accuracy and reliability of the numerical methods for the TSTO hypersonic stage separation, and the CFD simulations of the LSS for TSTO will be further compared and validated by the LSS test in the current study.

IV. RESULTS AND DISCUSSION

A. TSTO aerodynamic performance

Figure 13 shows the Mach 7 flows over the booster and the TSTO vehicle of the experimental Schlieren photo and the numerical Schlieren photo (i.e., the contour of the density gradient), and Fig. 14 plots the corresponding cases' pressure coefficient along the booster of the experiment and simulation results. As shown in Fig. 13(a), the leading edge shock attaches to the booster comprises the underneath strong oblique shock and upper weak oblique shock, resulting in high

pressure on the booster's lower surface, while low pressure on the booster's upper surface, as shown in Fig. 14. Moreover, the weak orbiter shock is attached on the orbiter's nose in the TSTO vehicle, as shown in Fig. 13(b). Additionally, with the increase in the AoA, the pressure on the booster's lower surface increases with stronger leading edge shock, while the pressure on the booster's upper surface decreases a little. In addition, after comparing the shock structure and the pressure coefficient along the booster of the experiment and simulation results, they obtained good agreement with each other so that the reliability and accuracy of the CFD and testing measurement have been validated to some extent.

Table III displays the aerodynamic characteristics of the booster measured by the balance in the tests and computed from the simulations, in which the C_D , C_L , and C_M are calculated by Eqs. (23)–(25), where “*” can be replaced by “o” and “b” for the orbiter and the booster, respectively. Where D is the drag, L is the lift, and M_z is the pitching moment ($M_z > 0$ indicates the pitch-up moment, and $M_z < 0$ indicates the pitch-down moment). The lift-to-drag ratio of the booster

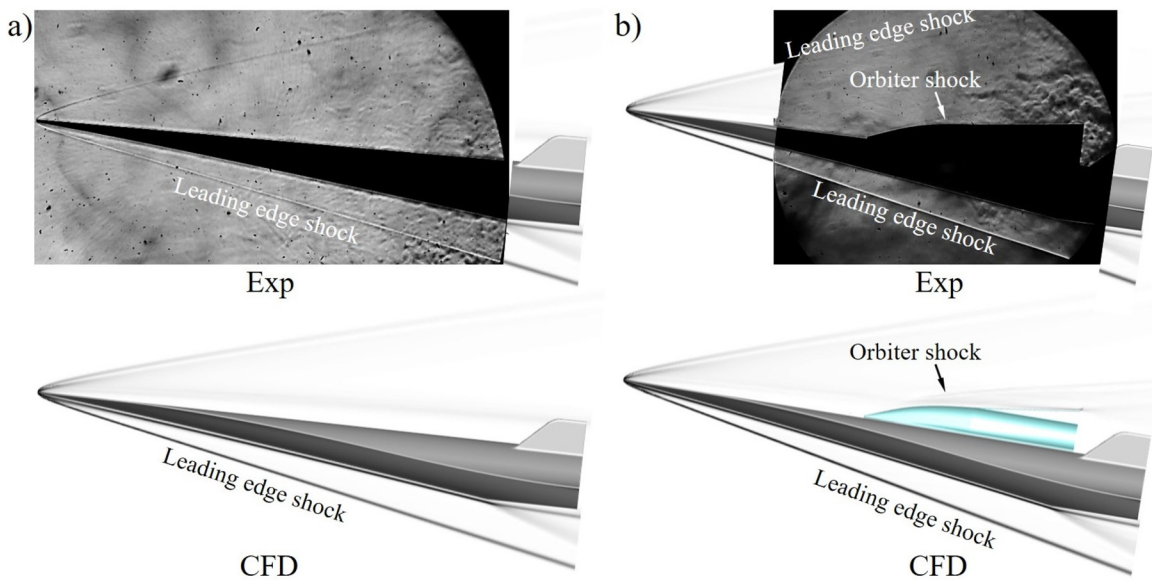


FIG. 13. Comparison of Schlieren photos of the booster (a) and the TSTO vehicle (b) between the experiments (upper) and CFD simulations (lower).

11 January 2024 04:54:41

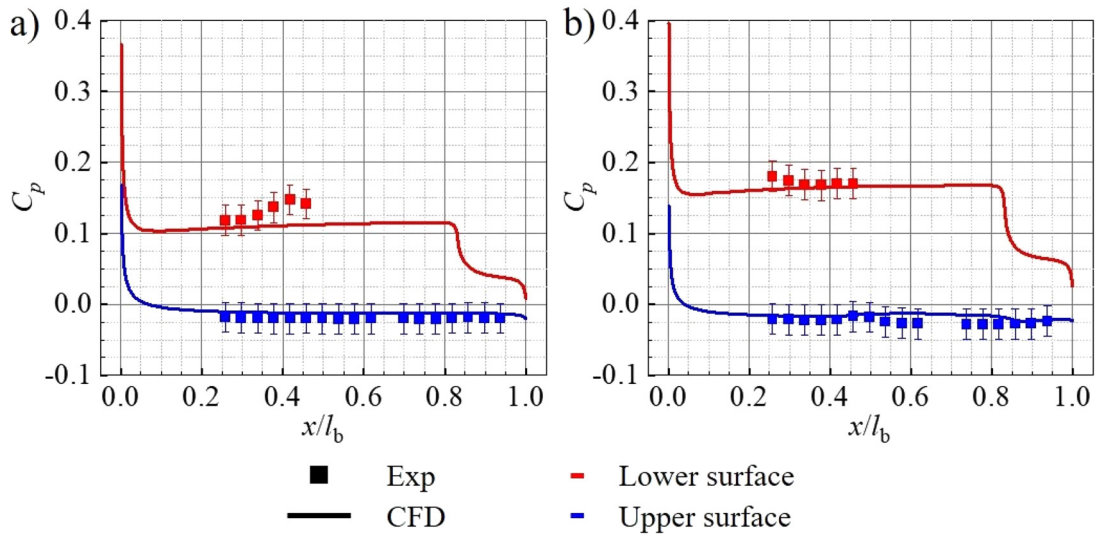


FIG. 14. Comparison of the pressure coefficient along the booster at the No. 1 case (a) and the No. 2 case (b) between the experiments and CFD simulations.

at $AoA = 5$ deg and the TSTO vehicle at $AoA = 8.1$ deg can reach higher than 3.7 and 3.2, respectively, which indicates the good aerodynamic performance of the TSTO vehicle. Moreover, the discrepancy in the aerodynamic coefficients between the experiment and simulation results just exists on the last digit after the decimal point, and it will be decreased as the AoA increases. Moreover, the discrepancy in the lift-to-drag is around 2% and the discrepancy in C_M approaches zero. However, the discrepancy in the C_D and C_M looks more evident, which may be because of the deviation of the base drag associated with the recirculation region in the booster’s wake between the measurement and CFD simulations. Nonetheless, the aerodynamic coefficients between the tests and the CFD simulations can be believed to be in good agreement with each other

$$C_D = \frac{D}{\frac{1}{2} \rho_\infty U_\infty^2 l_* w_*}, \quad (23)$$

$$C_L = \frac{L}{\frac{1}{2} \rho_\infty U_\infty^2 l_* w_*}, \quad (24)$$

TABLE III. Comparison of the aerodynamic characteristics of the TSTO vehicle.

No.	Test case		C_D	C_L	C_M	Lift-to-drag ratio
1	Booster	Exp	0.016	0.060	0.010	3.75
		CFD	0.018	0.069	0.010	3.83
		Discrepancy	11%	13%	0	2%
2	TSTO	Exp	0.029	0.095	0.014	3.26
		CFD	0.030	0.099	0.014	3.30
		Discrepancy	3%	4%	0	1%
		Discrepancy = $ \text{Exp} - \text{CFD} / \text{CFD} \cdot 100\%$				

$$C_M = \frac{M_z}{\frac{1}{2} \rho_\infty U_\infty^2 l_* w_*}. \quad (25)$$

B. Unsteady interactions in LSS

The unsteady interstage interaction in LSS for test cases No. 3 and 4 are investigated by the corresponding experiments and simulations. The independent variable for comparatively investigating the unsteady flowfields and wall pressure distribution is longitudinal displacement rather than the time so that both flowfields can be studied and validated with each other at the nearly same relative position for two stages. Although the separating sequences of LSS for the test and simulation are out of sync due to the forces on the body in its situation not being the same between the experiment and CFD, the simulations have been performed to approach the test in terms of the separating speed.

Figure 15 plots the typical flowfield of the TSTO vehicle during LSS of the numerical results. The numerical result shows the invisible flow information in the experimental Schlieren photo, i.e., Fig. 13(b), which includes the large subsonic area downstream of the orbiter, the shear layer developing downstream progressively, and the tail shock structure. Furthermore, the developed shear layer with high-speed impinges on the booster’s tail results in the pressure rise. Moreover, the Mach number contour lines show that the leading edge shock develops along the booster’s leading edge. Even though the clearance is observed due to the AoA , the TSTO still has good wave-riding performance and a high lift-to-drag ratio.

1. Small interstage gap interaction case at $AoA = 8.3$ deg

Figure 16 shows the typical flowfield between the test and the CFD simulation of the LSS at $AoA = 8.3$ deg. Due to the relatively low-density test flow environment in the JF-12 shock tunnel, the shock

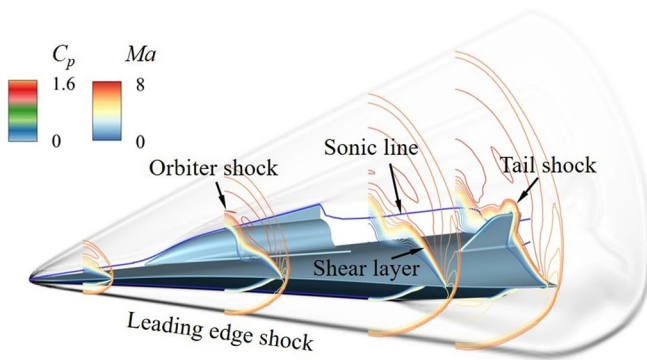


FIG. 15. Flowfield around the TSTO vehicle at $\Delta x/l_0 = -0.49$ during LSS at $AoA = 8.3$ deg (numerical Schlieren at symmetry and end plane, pressure coefficient contour on stages' surface, and several Mach number contour lines).

waves are not easily observed even though presented Schlieren photos have been processed to increase the contrast ratio. Thus, the supplementary numerical Schlieren photos in the corresponding case can present the dynamic shock wave structures clearly as a reference for the test in the LSS. Moreover, the white points shown in the experimental Schlieren are the LEDs to be taken as the trajectory markers. As shown in Fig. 16, the test captured the most important part of the separation process, i.e., phase II shown in Fig. 7. Moreover, the separation process and the variation of the shock wave structures during LSS are nearly the same between the test and the CFD. Both results show that the orbiter separates from the booster smoothly and successfully. Moreover, the interstage gap maintains the zero during phase I, i.e., $\Delta x/l_0 \geq -1.13$; then, it gradually increases to a small value under the aerodynamics induced by interstage shock waves in phase II, i.e., $-1.13 \geq \Delta x/l_0 > -2.16$; and finally, the successfully separated orbiter flights forward freely. During LSS, the flowfield around TSTO is governed by the type I and VI SSI,⁴⁸ while the interstage gap is zero and shock

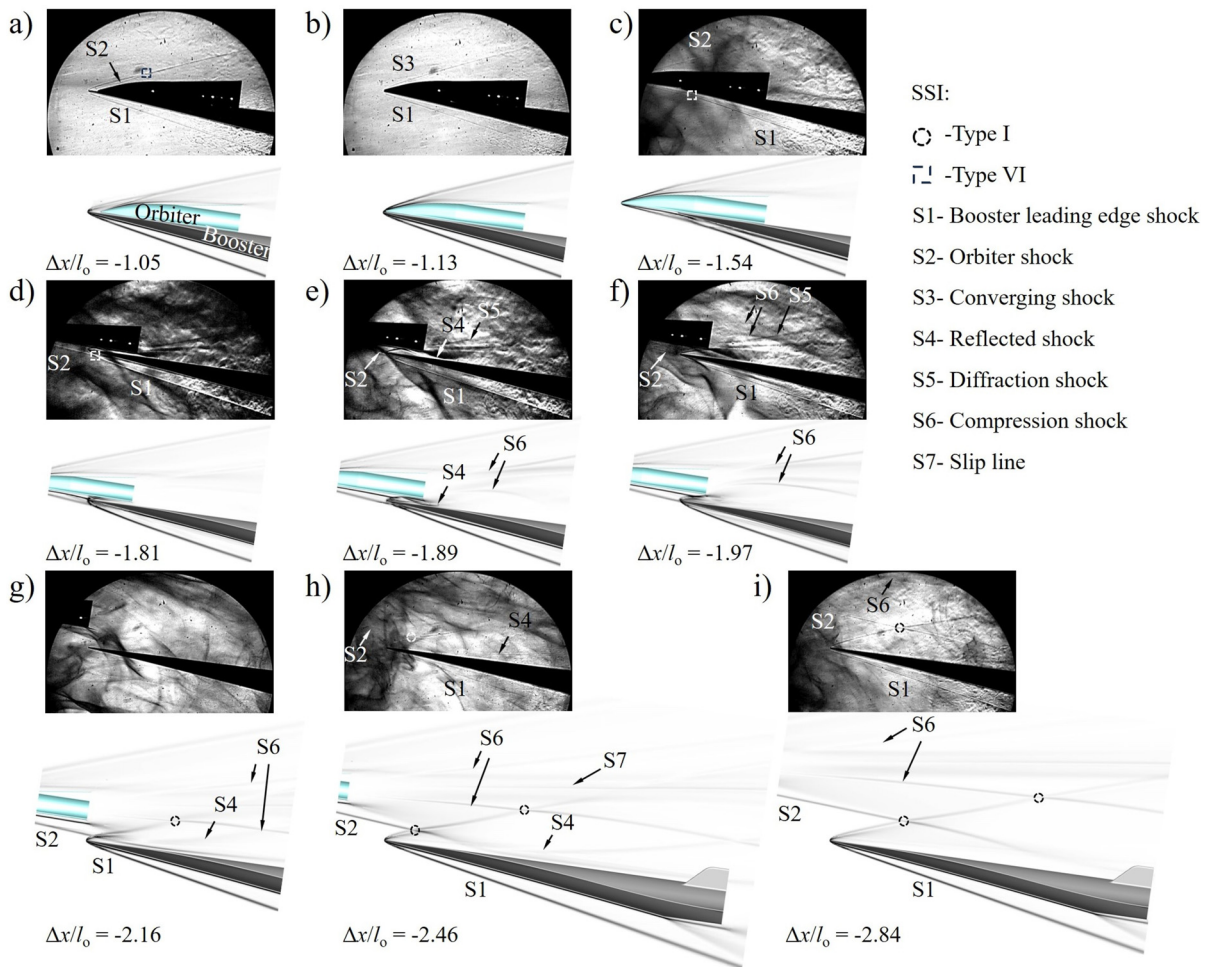


FIG. 16. The typical flowfields during LSS at $AoA = 8.3$ deg of experimental Schlieren photos (upper subgraph) and numerical Schlieren photos (lower subgraph).

reflection and is increasing. In phase I, neither the interstage gap nor the shock reflection is observed in the Schlieren photos; the flowfield is characterized by the booster leading edge shock S1 and the orbiter shock S2 as shown in Fig. 15. Moreover, as the separation progresses, the S1 and S2 occur with type VI SSI as shown in Fig. 16 until the upper part of the S1 and the S2 converges into the converging shock S3 when the leading edge of both stages coincidence, as shown in Fig. 16(b). The S3 degenerates into S2 at once when the orbiter breaks through the S1, and the S2 interacts with the S1 of type VI SSI underneath the orbiter, as shown in Fig. 16(c). Moreover, the exposure of the orbiter in the freestream causes the lift and the pitching moment to increase and overcome the gravity so that the interstage gap occurs, as shown in Fig. 16(d). Then, S1 starts to dominate the interstage interaction and affects the stages' aerodynamics. As shown in Fig. 16(e), the S1 impinges on the orbiter's lower wall and reflects between the interstage wall resulting in the reflected shock S4. As the separation proceeds, the interstage gap increases further, and the S1 impinges on the tail of the booster's lower wall without shock reflection so that S4 disappears, as shown in Fig. 16(f). Moreover, the diffraction shock S5 of the booster and the compression shock S6 are observed in the wake of the orbiter as shown in Figs. 16(e) and 16(f). S1 no longer interacts with the orbiter when the orbiter has separated from the booster; it interacts with the compression shock S6 of the type I SSI in the orbiter's wake, as shown in Fig. 16(g). Moreover, the orbiter shock S2 transits from the type VI SSI with the S1 and then impinges on the

booster's leading edge and now interacts with the S1 of type I SSI. The transmitted shock of the S2 impinges on the booster and causes the formation of the reflected shock S4, as shown in Figs. 16(g) and 16(h). With the flying forward of the orbiter, S4 moves downstream with a decreasing strength along the booster; finally, S2 no longer reflects on the booster; the flowfield around TSTO only remains the type I SSI of the S1 with the orbiter shock and the compression shock in the orbiter's wake.

Figure 17 plots the pressure coefficient along the stages' wall during LSS of the experiment and CFD simulations at corresponding instants as shown in Fig. 16. Moreover, Figs. 18 and 19 plot the pressure coefficient contours and skin-friction lines on the orbiter's lower wall and the booster's upper wall at the corresponding representative instants of the CFD simulation. Although the installed pressure transducers only can capture the part positions along the boosters' upper and lower walls, the numerical results in conjunction with the tested results provide the complete pressure coefficient distribution to reflect the variations of the interstage shock structure and aerodynamics.

As shown in Fig. 17, the fluctuation of the wall pressure coefficient mainly occurs on the first part of the booster's upper wall and the rear part of the orbiter's lower wall where the interstage interaction plays a role when the orbiter is breaking through the booster's leading edge shock. When the orbiter slides on the booster's upper wall, the obstruction of the orbiter's nose will increase the local booster's wall pressure slightly, such as $\Delta x/l_o = -1.05$. When $\Delta x/l_o = -1.13$, the

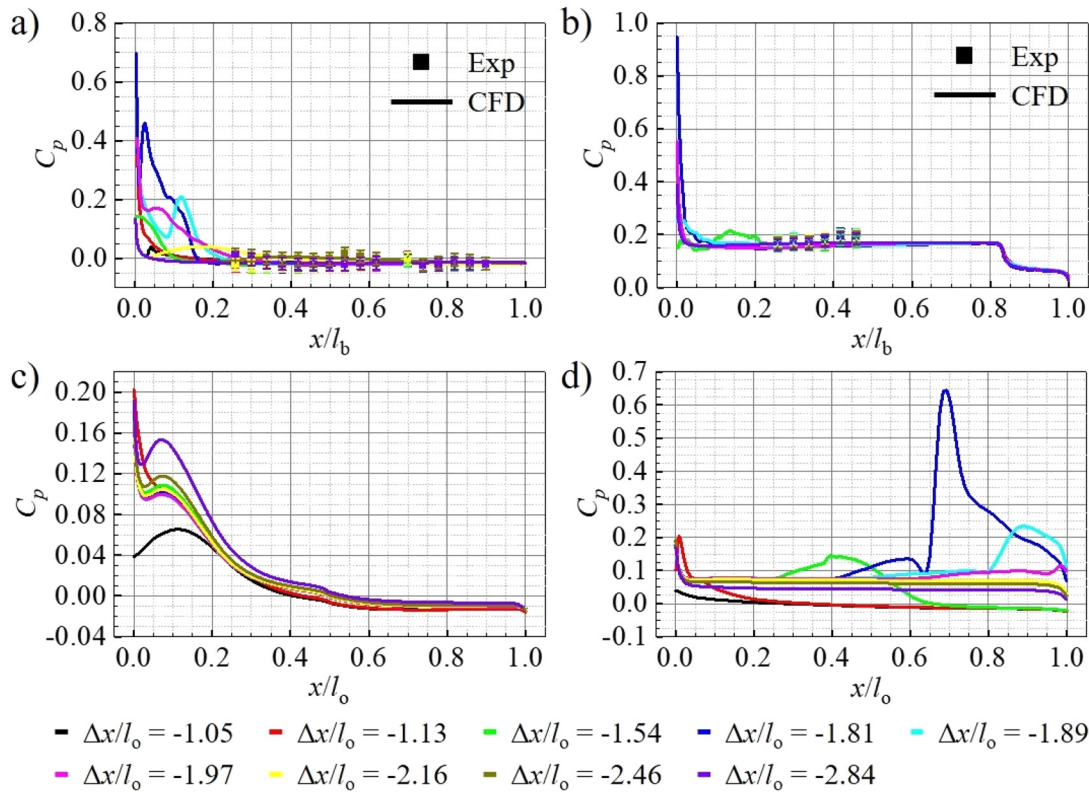


FIG. 17. Comparison of the pressure coefficient along the stages' wall: (a) booster's upper wall, (b) booster's lower wall, (c) orbiter's upper wall, and (d) orbiter's lower wall between the experiment and the CFD simulation for LSS at AoA = 8.3 deg.

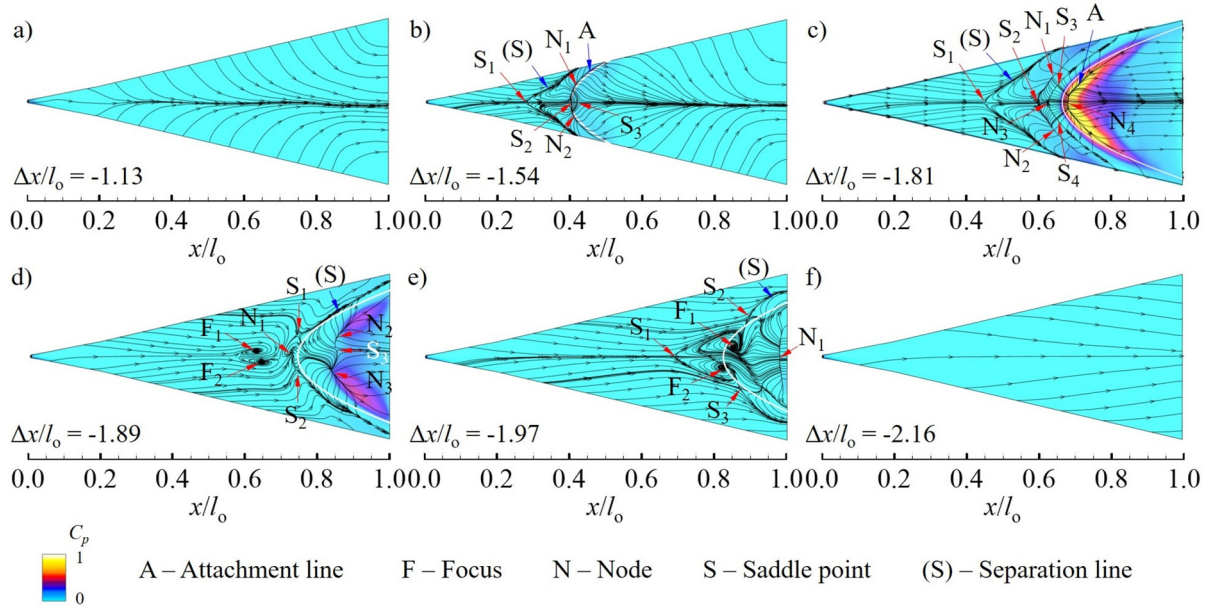


FIG. 18. Typical pressure coefficient contours and skin-friction lines on the orbiter's lower wall at some instants during LSS at AoA = 8.3 deg (white line in each subgraph denotes the outline of the booster's leading edge).

convergence of the S1 and S2 would increase the pressure coefficient along the orbiter's upper wall, as shown in Fig. 17(c). Since nearly no interstage interaction while the orbiter is sliding on the booter, there is no recirculation induced by the shock nor the adverse pressure gradient of the interstage flow, as shown in Fig. 18(a). When the orbiter breaks through S1, the shear layer of the booster impinges on the underneath of the booster's nose causing the pressure to rise, such as $\Delta x/l_o = -1.54$, as shown in Fig. 17(b); with the lifting of the orbiter, the interaction area between the orbiter's shear layer and the booster across the leading edge, for example, at $\Delta x/l_o = -1.81$, the shear layer impinges on the leading edge and result in the nearby pressure to rise highly, as shown in Figs. 17(a) and 17(b). Additionally, before the orbiter detaches from the booster completely, the booster's leading edge obstructs the airflow underneath the orbiter so that the flow separates under the shear layer and engenders a recirculation region on the

orbiter's lower wall, i.e., $\Delta x/l_o = -1.54$, as shown in Figs. 16(c) and 18(b). Moreover, the flow obstruction of the booster's leading edge will induce a small recirculation zone upstream of the leading edge, resulting in a multi-saddle-node separation topological structure. The separation line (S) and the reattachment line A together envelope the recirculation zone, and the attachment line nearly develops along the leading edge coincidentally, as shown in Fig. 18(b). The interaction effect of the booster's leading edge on the orbiter is not only manifested in the obstruction to the flow but also in the fact that S1 will impinge on the orbiter's lower wall, leading to an increase in wall pressure. As shown in Fig. 17(d), the pressure coefficient along the orbiter's wall increases due to the obstruction of the booster and the booster's leading edge shock, such as $\Delta x/l_o = -1.54$, -1.81 , and -1.89 . In particular, the pressure along the orbiter's lower wall will increase twice due to the interaction effect of the booster's leading edge when $\Delta x/l_o = -1.81$

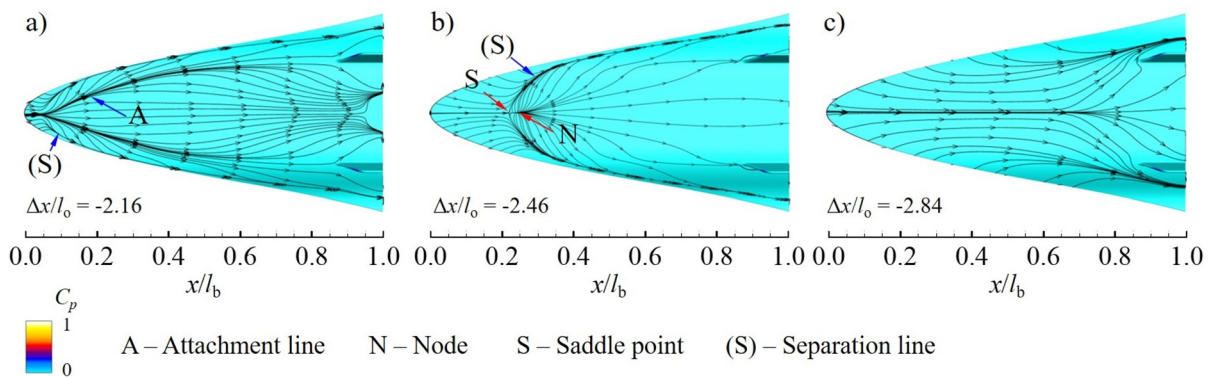


FIG. 19. Typical pressure coefficient contours and skin-friction lines on the booster's upper wall at some instants during LSS at AoA = 8.3 deg.

11 January 2024 04:54:41

as shown in Fig. 17(d). The twice pressure rise and the interaction of the booster's leading edge shock together induce the more complex recirculation region and separation topology on the orbiter's lower wall as shown in Fig. 18(c). First, the separation saddle point S_1 , the reattachment saddle point S_2 , and two reattachment nodes N_1 and N_2 , together with the separation line (S), comprise the first recirculation zone. Second, the separation node N_3 , two separation saddle points S_3 and S_4 , and reattachment N_4 , together with the reattachment line A, comprise the second recirculation zone. As the separation proceeds, the interstage gap increases, and S_1 is reflected on the orbiter's lower wall with decreasing strength, so the obstruction effect to the interstage flow and adverse pressure is weak. The recirculation zone on the orbiter's lower wall varies, and the focuses are introduced into the separation topology as shown in Figs. 18(d) and 18(e). At last, the recirculation zone vanishes on the orbiter's lower wall as shown in Fig. 18(f) once the orbiter detaches from the booster so that no interaction effect of the booster's leading edge on the orbiter. In addition, the booster will be influenced by the orbiter shock even though the shock strength is weak and the wall pressure increases slightly, as shown in

Fig. 17(a) such as at $\Delta x/l_o = -2.16$ and -2.46 . However, the incident shock S2 still induces the small-scale flow separation from the bypass separation envelopes by the separation line (S) and the reattachment line A at $\Delta x/l_o = -2.16$ to the downstream smaller and smaller recirculation zone comprising the separation saddle point S and the reattachment node N in the center at $\Delta x/l_o = -2.16$ as shown in Figs. 19(a) and 19(b). Finally, the recirculation zone vanishes, with the incident shock strength further decreasing as shown in Fig. 19(c), and the booster is nearly undisturbed.

2. Tiny interstage gap interaction case at AoA = 4.5 deg

Figure 20 presents the typical flowfields of the LSS at AoA = 4.5 deg in the test and the CFD simulation. The orbiter also accelerates along the booster with a zero interstage gap, as shown in Fig. 20(a), so the flowfield pattern around TSTO is similar to that in the AoA = 8.3 deg case, i.e., Figs. 16(a)–16(c). However, due to the lower AoA, the orbiter experiences a higher negative lift force compared to that in the AoA = 8.3 deg case; the orbiter cannot lift to the

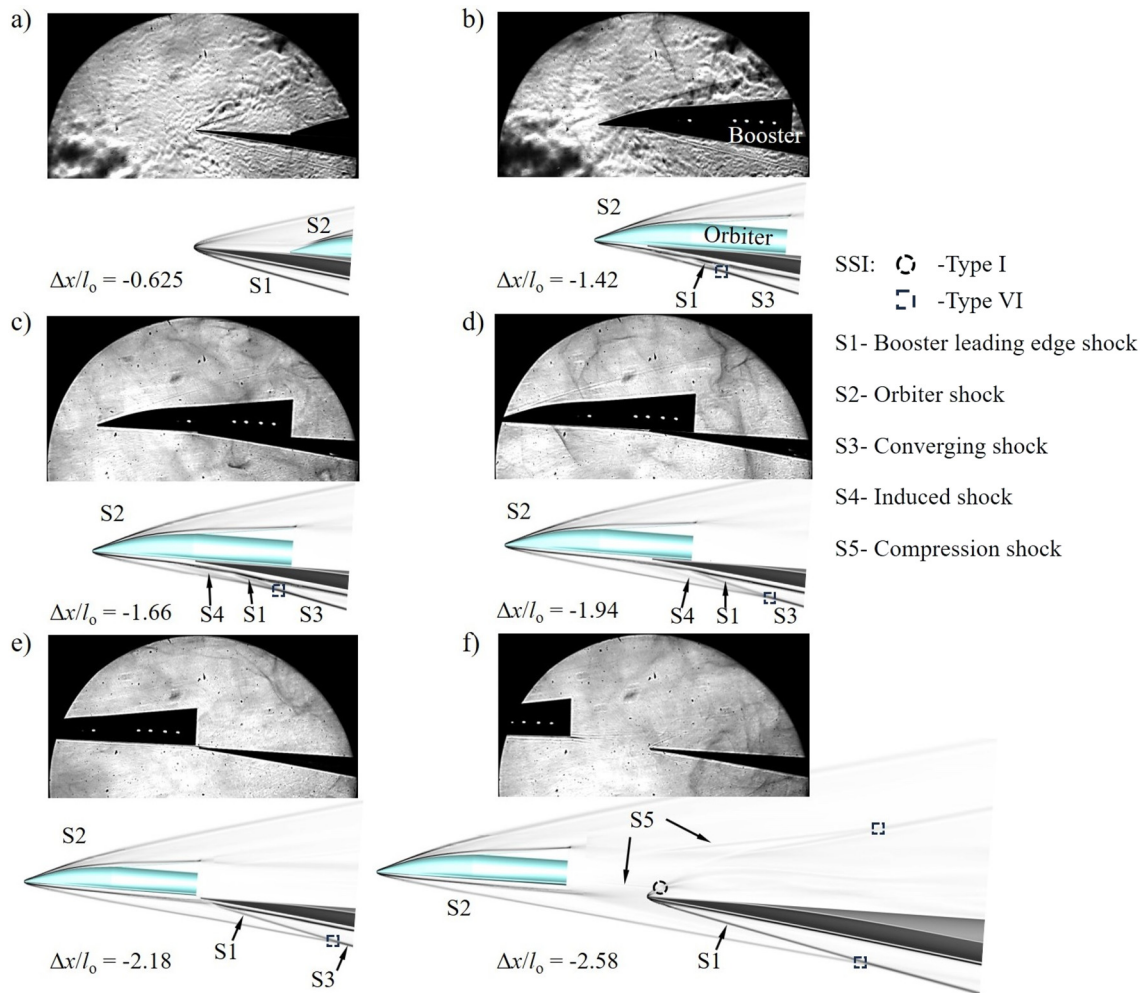


FIG. 20. The typical flowfields during LSS at AoA = 4.5 deg of experimental Schlieren photos (upper subgraph) and numerical Schlieren photos (lower subgraph).

11 January 2024 04:54:41

booster with the interstage gap during separation. Namely, the interstage gap maintains a zero or a tiny value in the whole separation, as shown in Figs. 20(a)–20(e). Therefore, neither the shock reflection nor the SBLI observed in the $\text{AoA} = 8.3$ deg case is introduced into the interstage at $\text{AoA} = 4.5$ deg; the interstage interaction is simple and weak during separation. Additionally, the orbiter's shear layer does not impinge on the booster's leading edge to bring the high-pressure load on it but develops along the booster's lower wall, as shown in Fig. 20(c). Moreover, the deflected shear layer will engender the induced shock S4 so that S4 and orbiter shock S2 together with the booster leading edge shock S1 converge into a strong shock S3, as shown in Figs. 20(c) and 20(d). After the orbiter separates from the booster, the orbiter's shear layer also detaches from the booster's lower wall, so that the induced shock S4 disappears as shown in Fig. 20(e). The flowfield remains the trip-wave structure in the type VI SSI form consisting of the S1, S2, and S3, as well as the booster isolated in the wake of the orbiter. The compression shock S5 interacts with S1 in type I SSI, and the transmitted shock of the S1 interacts with S5 in type VI SSI, as shown in Fig. 20(f). On the whole, the flowfield of the CFD result agrees well with that of the experimental result again at the lower AoA separation case and the tiny interstage gap determines the simpler and weaker interaction flowfield pattern during LSS for the TSTO vehicle given the wave structure in Schlieren results.

Figure 21 plots the CFD and experimental results of the wall pressure coefficient along both stages during LSS at $\text{AoA} = 4.5$ deg with the same plotting scale of graphs in Fig. 17 for the $\text{AoA} = 8.3$ deg case. First, the measured pressure coefficients along the booster's walls agree with the numerical results as shown in Figs. 21(a) and 21(b). Second,

the pressure coefficient along both stages' walls excludes the orbiter's upper wall lower than that in the case of the $\text{AoA} = 8.3$ deg. That is because the weaker stage interaction during LSS at lower AoA is associated with a tiny interstage gap compared to the higher AoA case. The peak pressure on the booster's leading edge vanishes at $\text{AoA} = 4.5$ deg case since the particular phenomenon that the orbiter's shear layer impinges on the booster's leading edge shown in Fig. 16(d) at $\Delta x/l_o = -1.81$ vanishes due to the tiny interstage gap as shown in Figs. 20(c)–20(e). After the orbiter detaches from the booster, the shear layer turns into the expansion fan flow over the booster's leading edge, as shown in Fig. 20(f). Thus, the pressure coefficient on the leading edge is not high. Moreover, little pressure rises on the booster leading edge as shown in Fig. 21(a) because of the obstruction to the flow in front of the leading edge. The pressure will decrease with the detaching of the orbiter from the booster as the flow obstruction effect vanishes at $\Delta x/l_o = -2.18$. In addition, the pressure increases near the nose on the booster's lower wall in Fig. 21(b) at $-2.18 < \Delta x/l_o \leq -1.81$ due to the compression of the weak induced shock S4 and the shifted booster leading edge shock S1 caused by the flow deflection between the shear layers of the orbiter and the booster, as shown in Figs. 20(b)–20(d). Since the lower AoA results in the stronger upper part of the orbiter shock S2, the pressure coefficient along the orbiter's upper wall is larger during LSS as shown in Fig. 21(c). Finally, the flow obstruction of the booster leading edge also induces the pressure to increase on the orbiter's lower wall during the detaching process even though the increment is small, as shown in Fig. 21(d). Furthermore, the pressure difference between upstream and downstream on the orbiter's lower wall decreases during the detaching process since the tiny interstage

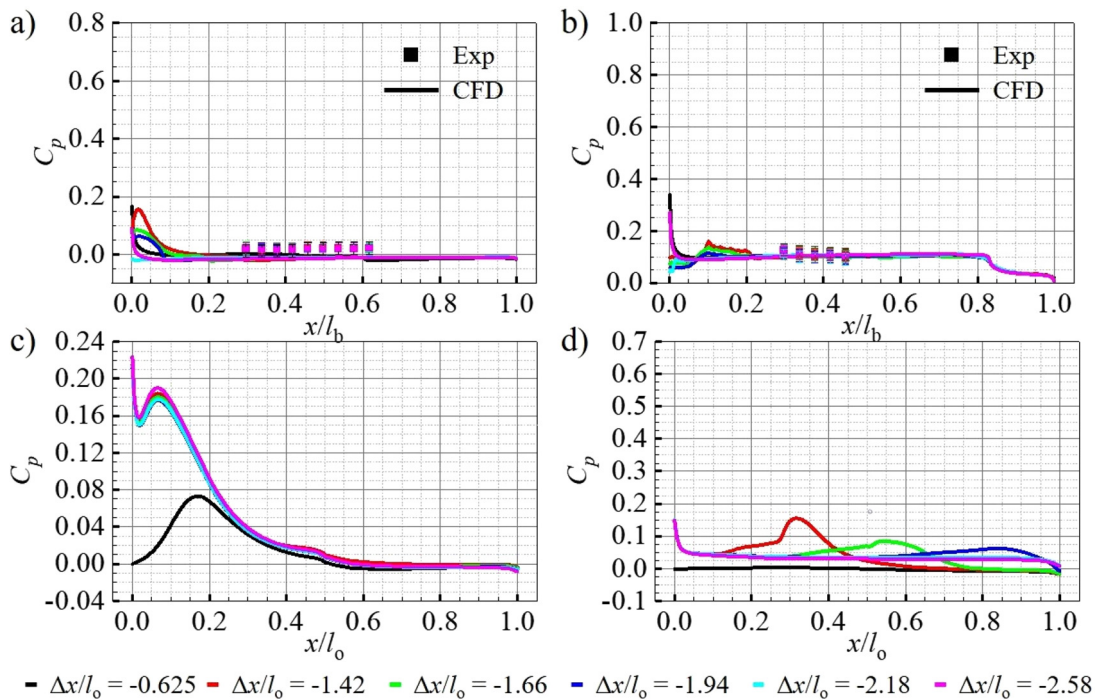


FIG. 21. Comparison of the pressure coefficient along the stages' wall: (a) booster's upper wall, (b) booster's lower wall, (c) orbiter's upper wall, and (d) orbiter's lower wall between the experiment and the CFD simulation for LSS at $\text{AoA} = 4.5$ deg.

gap flow length and the associated driver force for the downstream flow are decreasing. Since no interstage shock reflection occurs, no peak pressure rises on the orbiter's lower wall and the booster's upper wall during LSS.

C. Separation trajectory and unsteady aerodynamics

The non-dimensional orbiter's separation trajectories were captured in the Schlieren video and predicted by the CFD simulation for the LSS at AoA = 8.3 and 4.5 deg, which are illustrated in Fig. 22. Additionally, the error bands of the captured results are also shown. In general, the trajectory and the pitching angle of the orbiter are consistent in the variation tendency and small disparity between the captured and predicted results for different AoA cases. Figure 23 plots the unsteady aerodynamic coefficients of stages during LSS at AoA = 8.3 and 4.5 deg of the numerical results. Due to the huge challenge and difficulty block in front of the unsteady aerodynamics measurement in the hypersonic shock tunnel with a very short test duration and extreme test environment, accurate unsteady aerodynamics cannot be measured and extracted right now. Since the consistency and good agreement of the CFD and experimental results showed, i.e., flowfields (Schlieren photos and wall pressure) and separating trajectory, the unsteady aerodynamics of the numerical simulation are representatively discussed here.

As shown in Fig. 22, the displacements of the CFD and the experiment are in good agreement, but the disparity is observed when the orbiter is detaching from the booster ($\Delta x/l_o \leq -1.75$) and the orbiter's pitching angle varies. On the one hand, the angular displacement is more difficult than the linear displacement in the identification process; on the other hand, the error in the moment of inertia caused by the LED structure in the orbiter may also result in the disparity observed in the pitching angle as shown in Fig. 22(b). The trajectory results show that the interstage gap in the AoA = 4.5 deg case is smaller than that at the AoA = 8.3 deg case, which corresponds to the

Schlieren results. Due to the higher lift induced by the interstage interaction in the separation phase II as shown in Fig. 23(b), the transverse displacement is generated obviously between stages. In turn, the increasing interstage gap introduces a stronger aerodynamic interaction, i.e., interstage shock reflection as shown in Figs. 16(d)–16(f), resulting in the larger aerodynamics as shown in Figs. 23(b) and 23(c). For example, the direct impingement of the booster leading edge shock brings drastic pressure on the orbiter's lower wall around $\Delta x/l_o = -1.81$, as shown in Figs. 16(d) and 18(c), so the lift force reaches a maximum as shown in Fig. 23(b). Furthermore, the interaction type is transferred into the shock reflection from the direct shock impingement, and the interaction strength decreases, so the pressure on the lower wall decreases resulting in the lift decreases. Therefore, the orbiter separates from the booster with a slightly higher transverse displacement at AoA = 8.3 deg as shown in Fig. 22(a). On the other hand, the pitching angle of the orbiter first slightly increases since the increasing nose-up moment is induced by the interaction effect of the booster's leading edge when the orbiter's nose breaks through the leading edge shock but then decreases due to the nose-down moment contributed by the high-pressure on the rear of the lower wall. Since the booster's leading edge shock interacts with the orbiter's lower wall at AoA = 8.3 deg, i.e., shock reflection occurs between stages as shown in Figs. 16(d) and 16(e), the orbiter experiences a greater pitching moment when the orbiter is detaching from the booster than that at AoA = 4.5 deg, as shown in Fig. 23(c). Meanwhile, the pitching angle of the orbiter at AoA = 8.3 deg varies at a greater rate than that at AoA = 4.5 deg as shown in Fig. 22(b). Particularly, the nose-down moment will decrease like the decreasing of the lift force when $\Delta x/l_o \leq -1.81$ at AoA = 8.3 deg since the interstage interaction occurring around the rear of the orbiter's lower wall becomes weak. Finally, the orbiter's pitching moment recovers to the undisturbed state (small nose-down moment) after detaching from the booster and is similar to the initial value, as shown in Fig. 23(c). Due to the nose-down moment after separation, the orbiter's lift, the pitching angle, and moment are

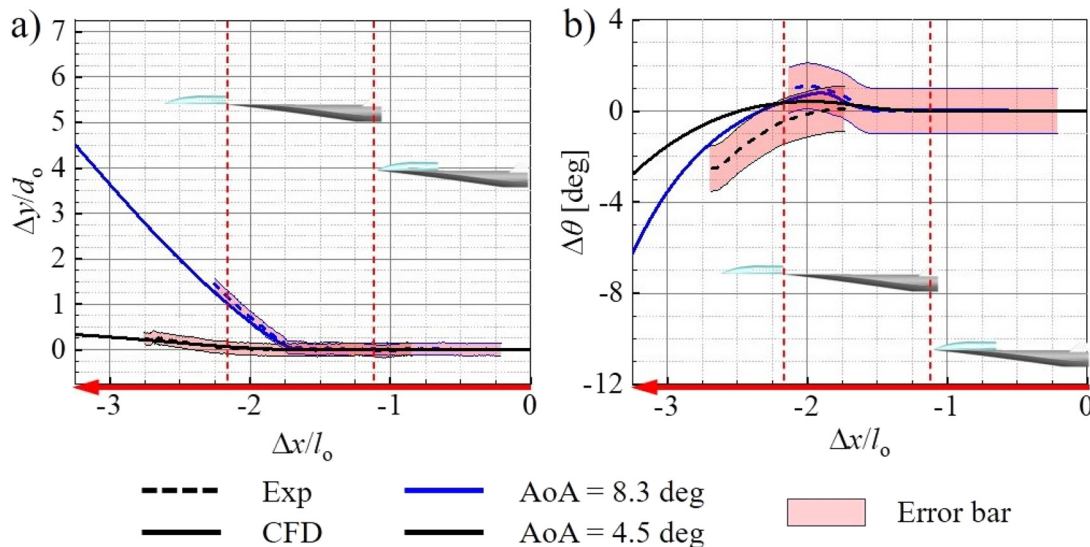


FIG. 22. The orbiter's linear displacement (a) and the angular displacement (b) of the experimental and numerical results for AoA = 8.3 and 4.5 deg.

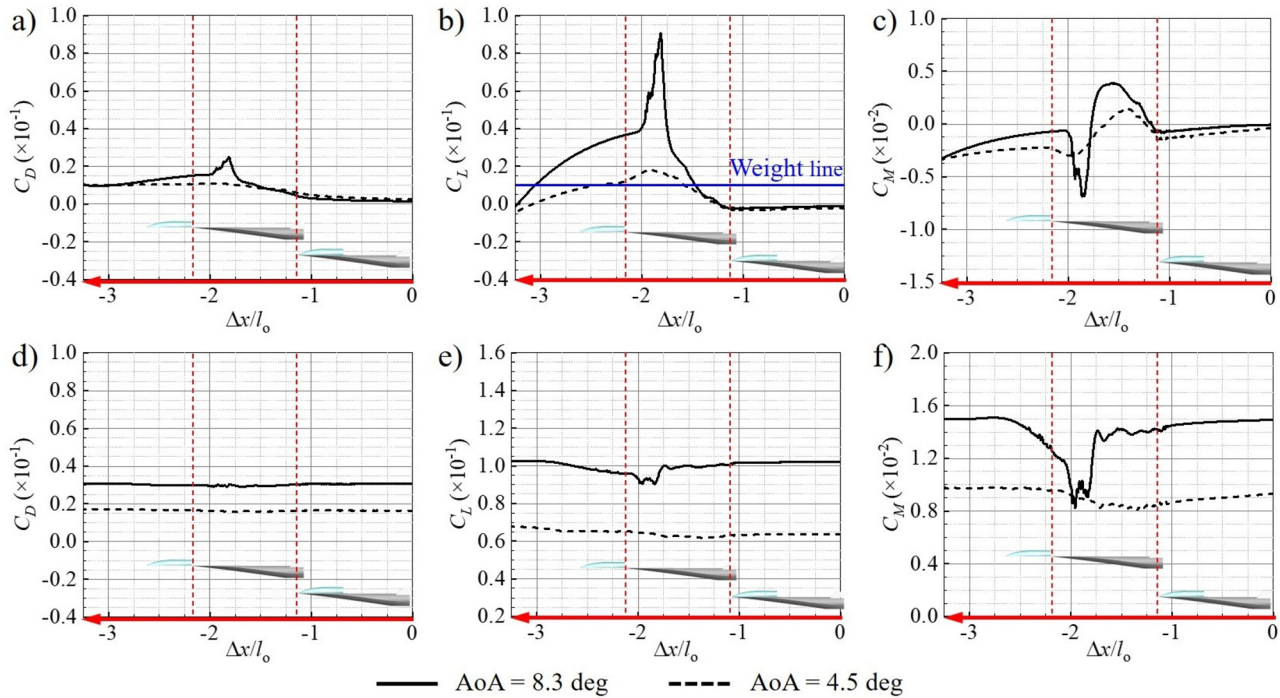


FIG. 23. The unsteady aerodynamic coefficients of the orbiter (a)–(c) and the booster (d)–(f) during LSS of numerical results for AoA = 8.3 and 4.5 deg.

decreasing. In addition, the drag coefficients for the orbiter at AoA = 8.3 deg and AoA = 4.5 deg are nearly varying similarly even though the drag coefficient shows a peak character due to the shock reflection, as shown in Fig. 23(a).

On the other hand, the drag and lift coefficients of the booster show more stable and smooth behavior compared to those of the orbiter, as shown in Figs. 23(a) and 23(b), and only a short-duration fluctuation can be observed when the orbiter is detaching from the booster. In other words, the lift and the drag performance will be maintained during LSS from the initial flight state. However, the pitching moment shows a notable and greater fluctuation at AoA = 8.3 deg. For example, the booster’s pitching moment decreases first due to the interstage shock reflection as shown in Figs. 16(d)–16(f) and then it starts to increase since the interstage shock reflection is replaced by the weaker reflection of the orbiter shock on the booster’s upper wall after the orbiter detaches from the booster as shown in Figs. 16(g) and 16(h). Finally, the pitching moment recovers into the undisturbed state with the shock reflection strength decreasing and disappears as shown in Fig. 16(i). In contrast, the pitching moment of the booster at AoA = 4.5 deg shows a more stable variation compared to that at AoA = 8.3 deg, as shown in Fig. 23(f). Moreover, the final state of the lift and pitching moment coefficients are slightly higher than the initial states since the leading edge shock above the booster is replaced by the weaker shock system downstream of the orbiter’s wake as shown in Figs. 20(e) and 20(f). Figure 24 presents the separation process of the TSTO at AoA = 8.3 and 4.5 deg captured by the high-speed camera II. The results directly show that the orbiter separates from the booster successfully in both cases and the interstage gap is small even tiny at a lower AoA condition. Moreover, the light around the stages

in Fig. 24 is the self-luminescence effect of hypersonic flow in the shock tunnel.

In general, the free-flight tests and numerical simulations together prove that the orbiter separates from the booster successfully and smoothly without stage collision and significant change in the attitude angle, the unsteady aerodynamic coefficients show that the orbiter is under a stronger interstage interaction at larger AoA, and the interstage interaction effect would be weaker at lower AoA with the tiny interstage gap. Moreover, the booster receives a smaller disturbance than that of the orbiter, which means the booster’s flight character would not be influenced obviously during LSS and advantages to the safety separation. Additionally, considering the weight of the orbiter model as shown in the blue line in Fig. 23(b), the lift might not offset the weight at lower AoA when the orbiter is detaching from the booster. Therefore, the suitable separation condition for the TSTO model during LSS may be the AoA slightly higher than 4.5 deg but lower than 8.3 deg to achieve enough lift to balance the weight but with weak interstage interaction for safety.

V. CONCLUSIONS

This paper investigates experimentally and numerically the unsteady interaction process of a parallel-staged TSTO vehicle during LSS at Mach 7 for different AoAs. The free-flight of the LSS experiments was conducted in the JF-12 shock tunnel, and some key test technologies and measurements, i.e., HPELS and the trajectory capture method, are presented in detail. The corresponding hypersonic flowfield around TSTO during LSS is also obtained by the laminar flow CFD simulations. Both unsteady interaction results are compared and analyzed in detail from the following aspects: flowfield pattern, wall

11 January 2024 04:54:41

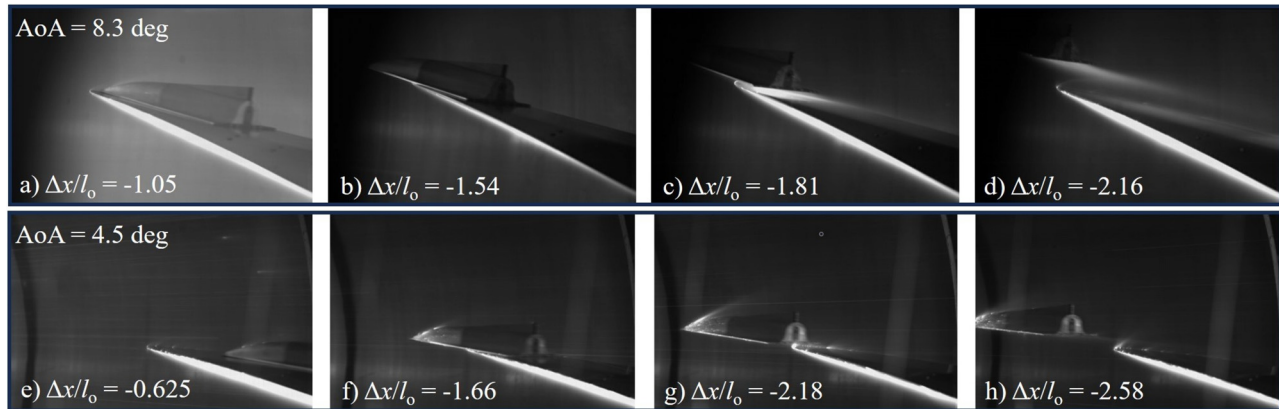


FIG. 24. The high-speed camera II photos of the LSS at the test of AoA = 8.3 deg (a)–(d) and AoA = 4.5 deg (e)–(h).

pressure, separation trajectory, and aerodynamics. The results are summarized as follows:

- (1) The experimental and numerical results are in good agreement with each other, and the qualitative and quantitative variables during LSS for different AoAs are consistent. In addition, the small disparity between the CFD and experimental results is also investigated.
- (2) The TSTO vehicle system has good aerodynamic performance, which has been validated by the CFD and the experiment: the booster and TSTO vehicles can achieve the high lift-to-drag ratio of 3.7 and 3.2, respectively.
- (3) The unsteady interaction mechanism during LSS involves the flowfield structure, the wall pressure, the flow separation, and aerodynamics at different AoAs, which are analyzed in detail. The unsteady interstage interaction during LSS becomes weaker with the smaller interstage gap at lower AoA. The LSS flowfield is dominated by the simple interaction type, such as type I and VI SSI as well as weak shock reflection with short duration. Moreover, the wall pressure and flow separation patterns show that the impingement of the booster leading edge shock and the orbiter's shear layer in the case of a small interstage gap will increase the complexity of the interaction during LSS, which is the main influencing factor determining the LSS behavior.
- (4) The free-flight LSS shows that the orbiter will have a nose-down tendency after detaching from the booster because the orbiter will recover to the initial tiny small nose-down moment state and the effect of the booster leading edge shock will be balanced as the orbiter separates from the booster. That is, the aerodynamic advantage of the LSS scheme. The aerodynamic interference for the two stages is weak at the lower AoA, and the booster experiences less disturbance during LSS than the orbiter. Both experimental and numerical results show that the two stages separate successfully and smoothly, further demonstrating the progressiveness and feasibility of the LSS scheme for the parallel-staged TSTO configuration. The favorable AoA condition for LSS of the TSTO vehicle may be slightly higher than 4.5 deg but lower than 8.3 deg.

ACKNOWLEDGMENTS

This study was co-supported by the National Natural Science Foundation of China (Nos. 11672357 and 11727901).

AUTHOR DECLARATIONS

Conflict of Interest

The authors have no conflicts to disclose.

Author Contributions

Yue Wang: Conceptualization (equal); Data curation (equal); Formal analysis (equal); Investigation (equal); Methodology (equal); Validation (equal); Visualization (equal); Writing – original draft (equal); Writing – review & editing (equal). **Yunpeng Wang:** Conceptualization (equal); Data curation (equal); Funding acquisition (lead); Methodology (equal); Project administration (equal); Resources (lead); Supervision (supporting); Writing – review & editing (equal). **Zonglin Jiang:** Funding acquisition (supporting); Project administration (supporting); Resources (supporting).

DATA AVAILABILITY

The data that support the findings of this study are available from the corresponding author upon reasonable request.

NOMENCLATURE

AoA	angle of attack (deg)
C_D	drag coefficient
C_L	lift coefficient
C_M	pitching moment coefficient
C_p	pressure coefficient
d	height of vehicle (m)
dt	dimensional time step (s)
D	drag force (N)
D_w	diameter of the observation window (m)
E	total energy per unit mass, $\text{J}\cdot\text{kg}^{-1}$

F_c	convective fluxes
F_x, F_y, F_z	force components exerted on the body, N
F_v	viscous fluxes
h	height of the center of gravity or the interstage gap (m)
H	enthalpy (MJ·kg ⁻¹)
I_{xx}	moment of inertia about the x -axis (kg·m ²)
I_{yy}	moment of inertia about the y -axis (kg·m ²)
I_{zz}	moment of inertia about the z -axis (kg·m ²)
k	slope of line
k_T	coefficient of thermal conductivity, W·(m·K) ⁻¹
l	length (m)
L	lift force (N)
m	mass (kg)
Ma	Mach number
M_x, M_y, M_z	moment components exerted on the body, N·m
M_z	pitching moment (N·m)
n	amounts of LEDs
p	pressure (Pa)
Re	unit Reynolds number (m ⁻¹)
t	time, s
T	temperature (K)
T_a	orbiter advance movement time (ms)
T_d	HPESL act delay time (ms)
T_e	effective test time (ms)
T_i	ignition trigger delay time (ms)
T_s	separation time (ms)
T_{td}	HPESL trigger delay time (ms)
U	speed (m·s ⁻¹)
u, v, w	velocity components in the $x, y,$ and z directions, m·s ⁻¹
v	speed of the orbiter (m·s ⁻¹)
V_g	contravariant velocity vector at the surface of the control volume, m·s ⁻¹
V_r	contravariant velocity vector relative to the motion of the grid, m·s ⁻¹
V_x, V_y, V_z	velocity components of the body, m·s ⁻¹
w	span of vehicle (m)
W	vectors of conservative variables
x	coordinate in the x direction (m)
y	coordinate in the y direction (m)
y^+	nondimensional wall spacing
α	initial pitching angle (deg)
$\Delta x, \Delta y, \Delta z$	displacement in the x, y, z direction, (m)
θ	pitching angle (deg)
Θ	heat conduction, W·m ⁻²
μ	coefficient of viscosity, N·s·m ⁻²
ρ	density (kg·m ⁻³)
τ_{ij}	component of viscous stress, N·m ⁻²
φ	sharp angle formed by two lines (deg)
$\omega_x, \omega_y, \omega_z$	angular velocity components of the body, rad·s ⁻¹

Subscripts

b	booster
i, j	count variables
o	orbiter
∞	freestream condition

REFERENCES

- 1S. Weingartner, "SAENGER - The reference concept of the German hypersonic technology program," AIAA Paper No. AIAA-93-5161, 1993.
- 2F. Chihiro, A. Kento, and H. Ogawa, "Fast and reliable prediction of scramjet flowfields via Gaussian process latent variable model and deep learning," *Phys. Fluids* **35**, 046120 (2023).
- 3L. McKinney, D. Farrell, T. Bogar, and J. Stemler, "Investigation of TSTO propulsion system options," AIAA Paper No. AIAA-2006-8054, 2006.
- 4Y. P. Wang, H. Ozawa, H. Koyama, and Y. Nakamura, "Abort separation of launch escape system using aerodynamic interference," *AIAA J.* **51**, 270–275 (2012).
- 5S. J. Laurence, N. J. Parziale, and R. Deiterding, "Dynamical separation of spherical bodies in supersonic flow," *J. Fluid Mech.* **713**, 159–182 (2012).
- 6V. Cardona and V. Lago, "Aerodynamic forces of interacting spheres representative of space debris re-entry: Experiments in a supersonic rarefied wind-tunnel," *Acta Astronaut.* **191**, 148–159 (2022).
- 7D. Peng, F. T. Xie, X. Liu, J. Z. Lin, Y. Z. Li, J. Zhong, Q. H. Zhang, and Y. Z. Liu, "Experimental study on hypersonic shock-body interaction between bodies in close proximity using translucent fast pressure- and temperature-sensitive paints," *Exp. Fluids* **61**, 120 (2020).
- 8Y. Wang, Y. P. Wang, and Z. L. Jiang, "Unsteady interaction mechanism of transverse stage separation in hypersonic flow for a two-stage-to-orbit vehicle," *Phys. Fluids* **35**, 056120 (2023).
- 9M. Patel and S. Navarro-Martinez, "Heat transfer to proximal cylinders in hypersonic flow," *Phys. Fluids* **35**, 036125 (2023).
- 10G. X. Xiang, C. Wang, H. H. Teng, and Z. L. Jiang, "Shock/shock interactions between bodies and wings," *Chin. J. Aeronaut.* **31**, 255–261 (2018).
- 11X. H. Fan, G. Wang, J. Z. Lin, Y. G. Yang, and Z. G. Tang, "Effects of expansion waves on incident shock-wave/boundary-layer interactions in hypersonic flows," *Phys. Fluids* **35**, 056121 (2023).
- 12G. Kumar and A. De, "Modes of unsteadiness in shock wave and separation region interaction in hypersonic flow over a double wedge geometry," *Phys. Fluids* **33**, 076107 (2021).
- 13F. Lozano, J. Saavedra, and G. Paniagua, "Aero-thermal numerical characterization of blunt fin-induced shock wave-boundary layer interaction and its control through leading-edge cooling injection," *Phys. Fluids* **34**(9), 096110 (2022).
- 14D. G. Wang, G. L. Han, M. K. Liu, and Z. L. Jiang, "Numerical investigation on unsteady interaction of oblique/bow shock during rotation based on non-inertial coordinate system," *Phys. Fluids* **34**, 121703 (2022).
- 15C. Weiland, *Aerodynamic Data of Space Vehicles* (Springer Science & Business Media, Berlin, 2014).
- 16W. Schroder and F. Mergler, "Investigation of the flowfield over parallel-arranged launch vehicles," AIAA Paper No. AIAA 93-3060, 1993.
- 17T. Cvrilje, C. Breitsamter, and B. Laschka, "Numerical simulation of the lateral aerodynamics of an orbital stage at stage separation flow conditions," *Aerosp. Sci. Technol.* **4**, 157–171 (2000).
- 18W. Schroder and G. Hartmann, "Analysis of inviscid and viscous hypersonic flows past a two-stage spacecraft," *J. Spacecr. Rockets* **30**, 8–13 (1993).
- 19M. A. Moelyadi, C. Breitsamter, and B. Laschka, "Stage-separation aerodynamics of two-stage space transport systems Part 2: Unsteady simulation," *J. Spacecr. Rockets* **45**, 1240–1250 (2008).
- 20W. Bordelon, A. Frost, and D. Reed, "Stage separation wind tunnel tests of a generic TSTO launch vehicle," AIAA Paper No. AIAA 2003-4227, 2003.
- 21H. Ozawa, K. Kitamura, K. Hanai, K. Mori, and Y. Nakamura, "Unsteady aerodynamic interaction between two bodies at hypersonic speed," *Trans. Jpn. Soc. Aeronaut. Space Sci.* **53**, 114–121 (2010).
- 22X. Q. Gong, H. Y. Jia, H. Zhao, J. Tang, J. Zhang, and Y. F. Fu, "Numerical simulation analysis on aerodynamic characteristics of TSTO interstage separation," *Acta Aerodyn. Sin.* **41**, 109–118 (2023). (in Chinese).
- 23J. Z. Lin, F. T. Xie, J. Zhong, D. Y. Zou, and Y. J. Pi, "Dual-body synchronous captive trajectory test technique in hypersonic wind tunnel," *Acta Aerodyn. Sin.* **41**, 77–86 (2023). (in Chinese).
- 24Y. Wang, Y. P. Wang, X. P. Xue, and Z. L. Jiang, "Numerical investigation on safe stage separation problem of a TSTO model at Mach 7," *Chin. J. Theor. Appl. Mech.* **54**, 526–542 (2022). (in Chinese).

- ²⁵Y. Wang, Y. P. Wang, and Z. L. Jiang, “Numerical investigation of aerodynamic separation schemes for two-stage-to-orbit-like two-body system,” *Aerosp. Sci. Technol.* **131**(Part A), 107995 (2022).
- ²⁶Y. Wang, Y. P. Wang, C. Wang, and Z. L. Jiang, “Numerical study of longitudinal stage separation for parallel-staged two-stage-to-orbit vehicle,” *Acta Aeronaut. Astronaut. Sin.* **44**, 127634 (2023). (in Chinese).
- ²⁷Y. Wang, Y. P. Wang, C. Wang, and Z. L. Jiang, “Numerical investigation on longitudinal stage separation of spiked Two-Stage-to-Orbit vehicle,” *J. Spacecr. Rockets* **60**, 215–229 (2023).
- ²⁸Y. Wang, Y. P. Wang, and Z. L. Jiang, “Experimental study of longitudinal stage separation of two-body configuration in shock tunnel,” *AIAA J.* **60**, 6940–6946 (2022).
- ²⁹Y. Wang, Y. P. Wang, and Z. L. Jiang, “Test technology of longitudinal stage separation for two-stage-to-orbit vehicle in shock tunnel,” *Acta Aeronaut. Astronaut. Sin.* **44**, 128126 (2023). (in Chinese).
- ³⁰Z. L. Jiang, “Experiments and development of long-test-duration hypervelocity detonation-driven shock tunnel (LHDst),” AIAA Paper No. AIAA-2014-1012, 2014.
- ³¹Y. P. Wang, Z. M. Hu, Y. F. Liu, and Z. L. Jiang, “Starting process in a large-scale shock tunnel,” *AIAA J.* **54**(4), 1240–1249 (2016).
- ³²M. K. Liu, G. L. Han, Z. X. Li, and Z. L. Jiang, “Experimental study on the effects of the cone nose-tip bluntness,” *Phys. Fluids* **34**(10), 101703 (2022).
- ³³Y. P. Wang, Y. F. Liu, and Z. L. Jiang, “Design of a pulse-type strain gauge balance for a long-test-duration hypersonic shock tunnel,” *Shock Waves* **26**(6), 835–844 (2016).
- ³⁴Y. P. Wang and Z. L. Jiang, “Impulse force-measurement system,” *Shock Waves* **30**(6), 603–613 (2020).
- ³⁵S. Chakravarthy, “A unified-grid finite volume formulation for computational fluid dynamics,” *Int. J. Numer. Meth. Fluids* **31**, 309–323 (1999).
- ³⁶E. F. Toro, *Riemann Solvers and Numerical Methods for Fluid Dynamics: A Practical Introduction* (Springer Science & Business Media, New York, 2009).
- ³⁷H. Luo, J. Baum, and R. Lohner, “Extension of HLLC scheme for flows at all speeds,” AIAA Paper No. AIAA 2003-3840, 2003.
- ³⁸J. R. Edwards, “An implicit multigrid algorithm for computing hypersonic, chemically reacting viscous flows,” *J. Comput. Phys.* **123**, 84–95 (1996).
- ³⁹M. K. Liu, G. L. Han, and Z. L. Jiang, “Experimental study on the evolution of mode waves in laminar boundary layer on a large-scale flat plate,” *Phys. Fluids* **34**, 013612 (2022).
- ⁴⁰H. Struchtrup, *Macroscopic Transport Equations for Rarefied Gas Flows: Approximation Methods in Kinetic Theory* (Springer Inc., Germany, 2005).
- ⁴¹Z. H. Wang, *Theoretical Modelling of Aeroheating on Sharpened Noses Under Rarefied Gas Effects and Nonequilibrium Real Gas Effects* (Springer thesis, Beijing, 2014).
- ⁴²Y. B. Gan, A. G. Xu, G. C. Zhang, Y. D. Zhang, and S. Succi, “Discrete Boltzmann trans-scale modeling of high-speed compressible flows,” *Phys. Rev. E* **97**, 053312 (2018).
- ⁴³Q. Z. Hong, J. A. Hao, K. C. Kit Uy, C. Y. Wen, and Q. H. Sun, “Thermochemical nonequilibrium effects on high-enthalpy double-wedge flows,” *Phys. Fluids* **34**, 063607 (2022).
- ⁴⁴M. H. Yu, Z. Y. Qiu, B. W. Zhong, and Y. Takahashi, “Numerical simulation of thermochemical non-equilibrium flow-field characteristics around a hypersonic atmospheric reentry vehicle,” *Phys. Fluids* **34**, 126103 (2022).
- ⁴⁵S. L. Tian, J. W. Fu, and J. T. Chen, “A numerical method for multi-body separation with collisions,” *Aerosp. Sci. Technol.* **109**, 106426 (2021).
- ⁴⁶M. S. Holden, M. MacLean, T. P. Wadhams, and A. Dufrene, “Measurements of real gas effects on regions of laminar shock wave/boundary layer interaction in hypervelocity flows for “blind” code validation studies,” AIAA Paper No. AIAA 2013-2837, 2013.
- ⁴⁷R. R. Heim, “CFD wing/pylon/finned store mutual interference wind tunnel experiment,” Report No. AEDC-TSR-91-P4, NASA, 1991.
- ⁴⁸B. E. Edney, “Effects of shock impingement on the heat transfer around blunt bodies,” *AIAA J.* **6**(1), 15–21 (1968).